Theses and Dissertations   1. Thesis and Dissertation Collection, all items

2012-09

Evaluation of Sun Glint Correction Algorithms for High-Spatial Resolution Hyperspectral Imagery

Miller, Chad I.

Monterey, California. Naval Postgraduate School

http://hdl.handle.net/10945/17421

NAVAL POSTGRADUATE SCHOOL

MONTEREY, CALIFORNIA

THESIS

EVALUATION OF SUN GLINT CORRECTION ALGORITHMS FOR HIGH-SPATIAL RESOLUTION HYPERSPECTRAL IMAGERY

by

Chad I. Miller

September 2012

Thesis Advisor: R.C. Olsen
Second Reader: Fred A. Kruse

Approved for public release; distribution is unlimited

THIS PAGE INTENTIONALLY LEFT BLANK

REPORT DOCUMENTATION PAGE		*Form Approved OMB No. 0704-0188*
Public reporting burden for this collection of information is estimated to average 1 hour per response, including the time for reviewing instruction, searching existing data sources, gathering and maintaining the data needed, and completing and reviewing the collection of information. Send comments regarding this burden estimate or any other aspect of this collection of information, including suggestions for reducing this burden, to Washington headquarters Services, Directorate for Information Operations and Reports, 1215 Jefferson Davis Highway, Suite 1204, Arlington, VA 22202-4302, and to the Office of Management and Budget, Paperwork Reduction Project (0704-0188) Washington DC 20503.

1. AGENCY USE ONLY *(Leave blank)*	2. REPORT DATE September 2012	3. REPORT TYPE AND DATES COVERED Master's Thesis
4. TITLE AND SUBTITLE Evaluation of Sun Glint Correction Algorithms for High-Spatial Resolution Hyperspectral Imagery		5. FUNDING NUMBERS
6. AUTHOR Chad I. Miller		

7. PERFORMING ORGANIZATION NAME(S) AND ADDRESS(ES)
   Naval Postgraduate School
   Monterey, CA 93943-5000
		8. PERFORMING ORGANIZATION REPORT NUMBER

9. SPONSORING /MONITORING AGENCY NAME(S) AND ADDRESS(ES) N/A		10. SPONSORING/MONITORING AGENCY REPORT NUMBER

11. SUPPLEMENTARY NOTES The views expressed in this thesis are those of the author and do not reflect the official policy or position of the Department of Defense or the U.S. Government. IRB Protocol number _____N/A_____.

12a. DISTRIBUTION / AVAILABILITY STATEMENT Approved for public release; distribution is unlimited	12b. DISTRIBUTION CODE A

13. ABSTRACT (maximum 200 words)
Sun glint correction algorithms were tested on a hyperspectral image containing cross-track sun glint. Spatial profiles of pixel radiance by pixel position were compared and slope values were calculated. The algorithms of Hedley et al., Lyzenga et al., and Joyce over-corrected for sun glint in the visible and near-infrared wavelengths. The method proposed by Kuster et al. was the weakest performer during visual comparison with the other method results. Spectral plots of corrected spectra to the original spectra were compared. Comparisons were performed on spectra from pixels with low and high amounts of sun glint. Spectra were compared within the sun glint corrected images and between the corrected images and the original image. Correlation values were calculated for each spectral comparison and averaged for each sun glint correction algorithm. The Lyzenga et al. sun glint correction algorithm had the highest average correlation value of 0.977 and is recommended for reducing sun glint in hyperspectral imagery when spectral integrity is required.

14. SUBJECT TERMS Remote Sensing, Hyperspectral, Sun Glint			15. NUMBER OF PAGES 99
			16. PRICE CODE

17. SECURITY CLASSIFICATION OF REPORT Unclassified	18. SECURITY CLASSIFICATION OF THIS PAGE Unclassified	19. SECURITY CLASSIFICATION OF ABSTRACT Unclassified	20. LIMITATION OF ABSTRACT UU

THIS PAGE INTENTIONALLY LEFT BLANK

EVALUATION OF SUN GLINT CORRECTION ALGORITHMS FOR HIGH-SPATIAL RESOLUTION HYPERSPECTRAL IMAGERY

Chad I. Miller
Civilian, Department of the Navy
B.S., Humboldt State University, 2003

Submitted in partial fulfillment of the
requirements for the degree of

MASTER OF SCIENCE IN REMOTE SENSING INTELLIGENCE

from the

**NAVAL POSTGRADUATE SCHOOL
September 2012**

Author: Chad I. Miller

Approved by: Dr. R.C. Olsen
                 Thesis Advisor

                 Dr. Fred A. Kruse
                 Second Reader

                 Dr. Dan Boger
                 Chair, Department of Information Sciences

THIS PAGE INTENTIONALLY LEFT BLANK

ABSTRACT

Sun glint correction algorithms were tested on a hyperspectral image containing cross-track sun glint. Spatial profiles of pixel radiance by pixel position were compared and slope values were calculated. The algorithms of Hedley et al., Lyzenga et al., and Joyce over-corrected for sun glint in the visible and near-infrared wavelengths. The method proposed by Kuster et al. was the weakest performer during visual comparison with the other method results. Spectral plots of corrected spectra to the original spectra were compared. Comparisons were performed on spectra from pixels with low and high amounts of sun glint. Spectra were compared within the sun glint corrected images and between the corrected images and the original image. Correlation values were calculated for each spectral comparison and averaged for each sun glint correction algorithm. The Lyzenga et al. sun glint correction algorithm had the highest average correlation value of 0.977 and is recommended for reducing sun glint in hyperspectral imagery when spectral integrity is required.

THIS PAGE INTENTIONALLY LEFT BLANK

TABLE OF CONTENTS

LIST OF FIGURES

THIS PAGE INTENTIONALLY LEFT BLANK

LIST OF TABLES

THIS PAGE INTENTIONALLY LEFT BLANK

LIST OF ACRONYMS AND ABBREVIATIONS

AISA	Airborne Imaging Spectrometer for Applications
AVIRIS	Airborne Visible/Infrared Imaging Spectrometer
BIL	Band Interleaved by Line
BIP	Band Interleaved by Pixel
BSQ	Band Sequential
cm^{-2}	1 / Square Centimeter
EMR	Electromagnetic Radiation
ENVI	ENvironment for Visualizing Images
FWHM	Full Width at Half Maximum
GSD	Ground Sample Distance
HSI	Hyperspectral Imaging
IDL	Interactive Data Language
μ	Micrometers
μm^{-1}	1 / Micrometer
m^{-2}	1 / Square Meter
MODTRAN	MODerate resolution atmospheric TRANsmission
MSI	Multispectral Imaging
mW	Milliwatts
nm	Nanometers
nm^{-1}	1 / Nanometer
NIR	Near Infrared
RGB	Red, Green, Blue
ROI	Region of Interest
sr	Steradians
sr^{-1}	1 / Steradian
SWIR	Short Wave Infrared
UTC	United Technologies
VIS	Visible
VNIR	Visible and Near Infrared
W	Watts
Wm^{-2}	Watts per square meter

THIS PAGE INTENTIONALLY LEFT BLANK

ACKNOWLEDGMENTS

THIS PAGE INTENTIONALLY LEFT BLANK

I.   INTRODUCTION

Remote sensing plays an integral role in improving our understanding of Earth's near-shore environments. Coastal remote sensing applications are widespread and varied. Optical remote sensing of coastal waters can be used to classify benthic habitat, determine bathymetry, and locate submerged mines. Littoral zone optical remote sensing offers unique challenges. One challenge that can potentially affect all coastal zone optical remote sensing applications is sun glint. Sun glint in remotely sensed optical imagery acts as a barrier to seeing into the water column.

Sun glint in imagery can incur large financial and scientific costs. Purchasing imagery from commercial satellite vendors is expensive, especially if sun glint has rendered some of the imagery unusable. Sun glint can create large errors in habitat classification and water depth measurements, corrupting scientific work. In the case of mine warfare, sun glint can lead to loss of life and property if mine detection is obscured by sun glint. Sun glint in imagery can be a serious challenge when using optical remote sensing for coastal zone management.

Sun glint correction methods are designed to reduce the effect of sun glint in imagery. Many of the sun glint correction methods take a multispectral imaging (MSI) approach to reducing the effect of sun glint even when applied to hyperspectral imagery. There has been less focus on hyperspectral imaging (HSI) and the impact sun glint correction has on the spectral integrity of corrected pixels.

This thesis follows the work of Kay et al. (2009) to test the performance of existing published sun glint correction methods, but extends their review of sun glint correction methods to include a ranking process based on how well the corrected spectra correlate to the original spectra. The intent of this thesis is to provide a recommendation on a sun glint correction method that reduces sun glint in hyperspectral imagery while maintaining spectral integrity for further spectral analysis.

1

THIS PAGE INTENTIONALLY LEFT BLANK

II.   BACKGROUND

A.   THEORY

1.   Electromagnetic Radiation

Light from the sun is the major source of incident radiation on Earth. Passive optical remote sensing detectors measure the incident radiation reflected or emitted from the Earth's surface. Electromagnetic radiation (EMR) can be described as a wave or a stream of photons (Mather 2004). When EMR is described as a wave, it is characterized by a certain wavelength from the electromagnetic spectrum. Humans have the ability to see EMR wavelengths from approximately 400 to 700 nanometers (nm) in the visible (VIS) portion of the electromagnetic spectrum. Within the VIS range of the electromagnetic spectrum, the human eye contains cones that are sensitive to red (~650 nm), green (~550 nm), and blue (~450 nm) portions of the electromagnetic spectrum (Olsen 2007). Therefore, human sight can be modeled with a mix of red, green, and blue (RGB) colors. In the field of remote sensing, the near-infrared (NIR) portion of the electromagnetic spectrum ranges from approximately 700 to 1,000 nm (Clark 1999). Together, visible and near-infrared (VNIR) make up the portion of the electromagnetic spectrum from approximately 400 to 1,000 nm. The short wave infrared (SWIR) region of the electromagnetic spectrum is approximately 1,000 to 2,500 nm. The hyperspectral test image for this thesis samples both VNIR and SWIR wavelengths.

2.   Statistics

A data set contains information about objects from a population. Objects can be characterized by variables. A data set can contain values for one or more variables of an object. The population of objects follows a distribution defining what values variables take and how often it takes these values. A distribution can be described by its shape, center, and spread (Moore et al. 2011). Most populations follow a normal, or Gaussian, distribution. This type of distribution can be described by its bell shaped curve where the center is at the peak of the curve and the spread represents the decreasing tails of the

curve from either side of the peak. The mean is the most common measure of a distribution's center and can be calculated by summing all values of a data set and dividing by the number of values in

$$\bar{x} = \frac{1}{n}\sum x_i ,$$ (1)

where $\bar{x}$ is the mean, n is the number of values in a data set, and x_i is the value at index i of the data set. The most common measure of spread in a distribution is the standard deviation. The standard deviation measures how far values are from their mean, where s^2 is the variance and the standard deviation s is the square root of the variance in

$$s^2 = \frac{1}{n-1}\sum (x_i - \bar{x})^2$$ (2)

$$s = \sqrt{\frac{1}{n-1}\sum (x_i - \bar{x})^2} .$$ (3)

Another important statistic of a population is the mode. The mode is the value that appears most often in a data set. It can be calculated by constructing a histogram of the data set and choosing the value with the highest frequency. It is possible to have more than one mode as in multimodal distributions. The above statistics are used in this thesis either directly in the sun glint correction algorithms or in the analysis of their results.

A scatterplot displays the relationship between two variables measured on the same object by plotting one variable on the horizontal x-axis and the other variable on the vertical y-axis (Figure 1). Each object's value in a data set is a point on the scatterplot. A scatterplot can show the form, direction, and strength of a relationship (Moore et al. 2011). The form can show a linear or curved relationship. The direction can indicate a positive or negative association between the variables. A positive association is observed when high values of both variables occur together and a negative association is when high values of one variable occur in conjunction with low values of the other variable. Strength shows how close points on the scatterplot lie to a form such as a line and

4

indicates how well the variables relate to each other. The correlation r measures the direction and strength of a linear relationship in

$$r = \frac{1}{n-1} \sum \left(\frac{x_i - \bar{x}}{s_x} \right) \left(\frac{y_i - \bar{y}}{s_y} \right),$$

(4)

where x is the x-variable and y is the y-variable of a scatterplot. The correlation value is between -1 and 1, where 0 indicates a very weak relationship, -1 and 1 indicates a very strong negative and a very strong positive relationship, respectively. Correlation is used in this thesis to examine the performance of sun glint correction algorithms. Figure 1 illustrates how correlation measures the direction and strength of a linear relationship.
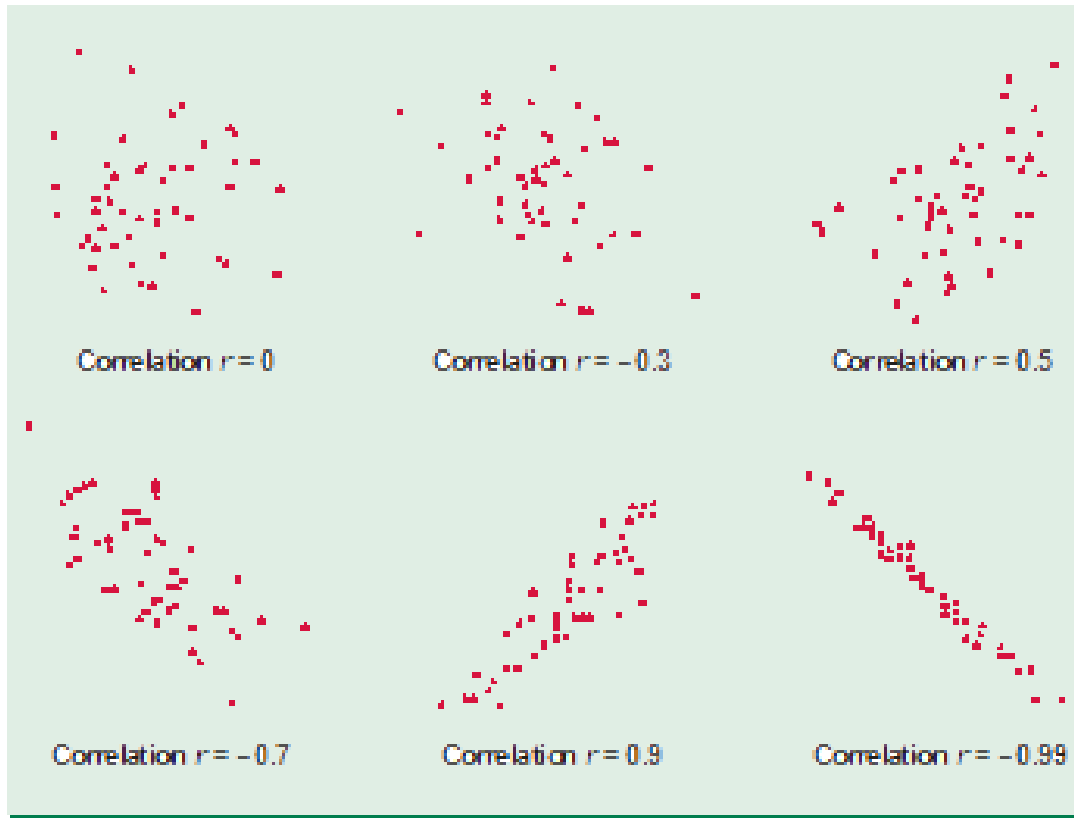
Figure 1.   Example of how correlation measures the direction and strength of a linear relationship. From Moore et al. (2011)

5

A least-squares regression line can be drawn on a scatterplot so that the sum of squares of the vertical distances of the data points from the line are as small as possible (Moore et al. 2011). The least-squares regression line $\hat{y}$ in

$$\hat{y} = b_0 + b_1 x \tag{5}$$

has a slope b_1 in

$$b_1 = r \frac{s_y}{s_x} \tag{6}$$

and a y-intercept of b_0 in

$$b_0 = \bar{y} - b_1 \bar{x}. \tag{7}$$

Scatterplots and least-squares regression can be used to determine the amount of sun glint in a pixel and are utilized in some published sun glint correction methods.

3.   Digital Image Data

A digital remote sensing imaging system uses optical lenses to collect light that is split into a variety of wavelengths from the electromagnetic spectrum and passes it onto a detector which records the information as pixels in a two-dimensional grid (Campbell 1996). The grid represents an image made of rows and columns of pixels. Each pixel contains an x and y coordinate specifying a location in image space and the data value of the pixel representing the quantity of EMR collected by the pixel. A single image displays pixel value quantities in shades of grey between black and white. Pixel locations in this thesis are specified using the (x, y) notation. The number of shades depends on the bit depth of the pixel which defines the radiometric resolution of the image (Richards and Jia 2006). For example, an 8-bit image has pixel values between 0 and 255, where 0 is black and 255 is white, with shades of grey in between. An 8-bit image is considered to have lower radiometric resolution than a 16-bit image where pixel values between 0 and 65,535 are allowed. The image utilized in this research has 16-bit radiometric resolution.

Multiple images, or image bands, depicting the same scene from different portions of the electromagnetic spectrum define MSI. Combining three image bands from the RGB portions of the electromagnetic spectrum into a composite creates a true-color image. A typical multispectral remote sensing imaging system includes at least 4 bands from the VNIR portion of the electromagnetic spectrum; 3 RGB bands and a NIR band. When the NIR band is displayed instead of the red band in a RGB composite, it is possible to see outside of the VIS portion of the electromagnetic spectrum. This is the case when vegetation appears bright red in false-color imagery because of the high reflectance of vegetation in the NIR portion of the electromagnetic spectrum. One technique this thesis utilizes to analyze the performance of sun glint correction algorithms involves graphically visualizing the result of 3 RGB bands and a NIR band of sun glint corrected hyperspectral images.

Hyperspectral imaging is when hundreds of image bands are collected simultaneously. The individual bands in a hyperspectral image cover smaller portions of the electromagnetic spectrum that, when combined, sample a larger contiguous portion of the electromagnetic spectrum. It is possible to derive a complete reflectance spectrum in each pixel of a hyperspectral image (Goetz et al. 1985). Each band of a HSI system samples a range of wavelengths from the electromagnetic spectrum. The wavelength range sampled, or band pass, is measured by the Full Width at Half Maximum (FWHM) of the sample's normal distribution (Swayze et al. 2003). This is considered the spectral resolution of a sensor and is normally stated as a single length for the entire image. Often the single stated length is a nominal length due to the fact that spectral resolution varies slightly between bands and is averaged over all bands of an image. The spectral resolution of an individual band can be given as a range between two FWHM wavelengths or as a single central peak wavelength. Most HSI systems place their band samples at intervals that completely sample a portion of the electromagnetic spectrum without gaps. Imaging spectrometry is the identification of features based on spectral signatures allowed by the high spectral resolution of HSI and the complete sampling of a portion of the electromagnetic spectrum. Figure 2 depicts how HSI can be conceptualized as a data cube in three-dimensional coordinate space where the x-axis and

the y-axis represent a single image band in the horizontal direction and the λ-axis represents the number of image bands at certain wavelengths in the vertical direction. Figure 2 also illustrates how imaging spectrometry can identify features in the image based on the spectral signature of a pixel.
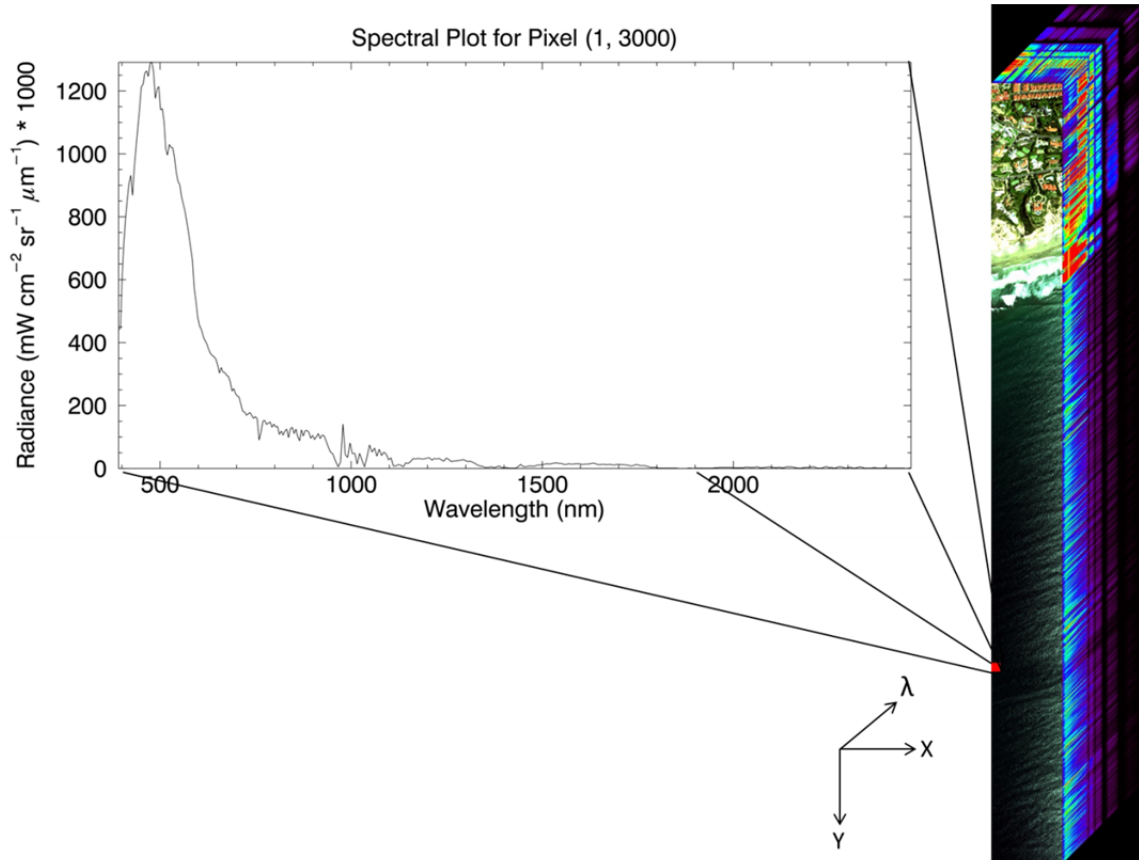
Figure 2.   Depiction of the test image as a three-dimensional data cube with the spectral plot for pixel (1, 3000).

Both multispectral and hyperspectral imagery data are stored by interleaving the column, row, and band dimensions of the data cube. The order in which the dimensions are stored differs by interleaving type. Image data stored by Band interleaved by pixel (BIP) are ordered by band, column, and row. Band interleaved by line (BIL) stores image data by column, band, and row. Band sequential (BSQ) stores image data by column, row, and band. The test image used in this thesis is in BIL format.

The size of objects that may be detected by a sensor is dependent on the spatial resolution of the imagery. Spatial resolution of imagery is the amount of detail that can be observed in an image (Gibson 2000). Higher spatial resolution imagery can resolve smaller objects. Image spatial resolution is limited by the Rayleigh criterion (Olsen 2007). The Rayleigh criterion is used to calculate the distance apart two objects need to be in order to be distinguished from each other. The calculation is based on the wavelength of EMR detected (λ), the diameter of the optical aperture (D), and the distance from the object (R) in

$$\Delta\theta = 1.22 \frac{\lambda R}{D}.$$
(8)

Spatial resolution of a digital remote sensing imaging system is defined by the Ground Sample Distance (GSD) or the distance on the ground between pixels. The image utilized in this research has a GSD of one meter.

4.   The Interaction of Electromagnetic Radiation with Matter

The interaction of EMR with matter can be described as the movement of light between two different media. The velocity of light changes as it is transmitted from one medium to another (Hecht 2001). The change of velocity of light in a medium is compared to the velocity of light in a vacuum to obtain the index of refraction for the medium in question. Snell's Law calculates the angle at which light is refracted when transmitted through a medium using both the index of refraction and the angle of incidence of light upon the medium (Feynman 1985). Light can be scattered off the surface of a medium in many unpredictable directions or absorbed by a medium and transferred as internal energy which is emitted as heat. Light can also reflect off a surface in a single, predictable direction with the angle of reflection equal to the angle of incidence. The Fresnel equations calculate the fraction of light reflected off the surface of a medium and the fraction of light transmitted through the medium (Mobley 1994). Light reflected off a smooth surface is called specular, or Fresnel, reflection and is the cause of sun glint in imagery.

9

5.   Electromagnetic Properties of Water

The atoms that comprise water molecules consist of electrons orbiting a nucleus. Electrons orbit the nucleus at discrete energy levels (Burns 1993). When a photon of a correct wavelength interacts with an atom, the electron is excited to a higher energy level and the photon is absorbed. If the electron falls to a lower energy level, a photon of a certain wavelength is emitted. The wavelengths of photons from the VIS portion of the electromagnetic spectrum do not contain the correct energy level to interact with the atoms of water molecules (Mobley 1994). Therefore, EMR from the VIS portion of the electromagnetic spectrum is not absorbed by the water molecule. The wavelengths of photons from the NIR portion of the electromagnetic spectrum contain the correct energy level to excite the electrons of the atoms and are absorbed by the water molecules. Water appears blue-green due to the blue-green wavelengths at the absorption minimum shown in Figure 3.
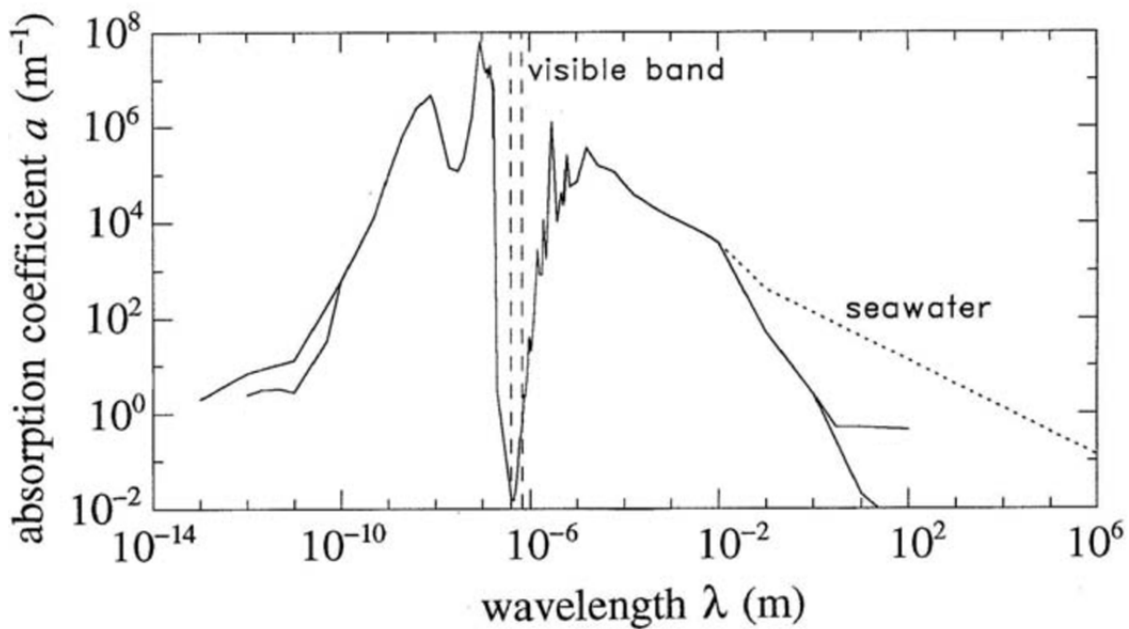
Figure 3.   Spectral absorption coefficient of pure water (solid line) and of pure sea water (dotted line) as a function of wavelength. The dashed line represents the VIS band. Modified from Mobley (1994).

Pure, optically deep water is a complete absorber of NIR EMR. Water is considered optically deep if it is deep enough that no EMR is reflected off of the bottom back through the water column and collected by the detector. Most natural waters are not pure and contain biological or inorganic materials suspended in the water column (Mobley 1994). Water will not absorb all NIR EMR if some NIR EMR is reflected off of material suspended in the water column. This causes natural waters to be a strong absorber of NIR EMR rather than a complete absorber of NIR EMR.

6. Radiometry

When EMR from the sun is described as photons, the energy of the photons incident on a unit of area of a plane perpendicular to and at a distance away from the sun can be calculated using the inverse square law. The inverse square law for irradiance states that the quantity or intensity of energy is inversely proportional to the square of the distance to the source of energy (Mobley 1994). Irradiance is the measurement of EMR from the sun at a given area of Earth in watts per square meter. At the top of the Earth's atmosphere irradiance is referred to as the solar constant and is roughly 1,367 W m^{-2} (Frohlich 1983). At the Earth's surface, downward irradiance is highly variable, based on the solar angle, and less than the solar constant due to the interaction of photons with atmospheric particulate matter. When EMR from a certain wavelength is measured, then irradiance becomes spectral irradiance and wavelength is included in the unit of measurement (W m^{-2} nm^{-1}).

Radiance describes the quantity of EMR emitted or reflected from a surface within a given solid angle in a specific direction. Solid angle is a two dimensional angle in three dimensional space that resembles a cone that originates from a point and projects a circular area on a surface (Mather 2004). Solid angle is important in remote sensing because it indicates the amount of upwelling EMR detected by a sensor through the optical system's aperture at its angle of view. Solid angle uses steradians (sr) as its unit of measurement. The unit of measurement for radiance is similar to irradiance but with the addition of the steradian unit for the solid angle (W sr^{-1} m^{-2}) and (W sr^{-1} m^{-2} nm^{-1}) for

spectral radiance. For this thesis, spectral radiance is the unit of measurement for pixel values in the image used to test sun glint correction algorithms and has a slightly modified form of (mW cm^{-2} sr^{-1} µm^{-1}).

7.   Imaging Spectrometry

The electromagnetic spectrum can be described as a continuous spectrum representing energy from a theoretical blackbody radiating at different wavelengths. Kirchhoff's law states that energy absorption is equal to energy emission for an object in thermal equilibrium (Chandrasekhar 1960). A blackbody is a perfect absorber of energy at all wavelengths and therefore is a perfect emitter of energy at all wavelengths. Planck's law calculates the amount of energy emitted at each wavelength by a blackbody. When blackbody radiation is plotted by wavelength, Planck's law states that the shape of the curve does not change as a function of temperature, only the amplitude and peak location of the curve changes as shown in Figure 4.
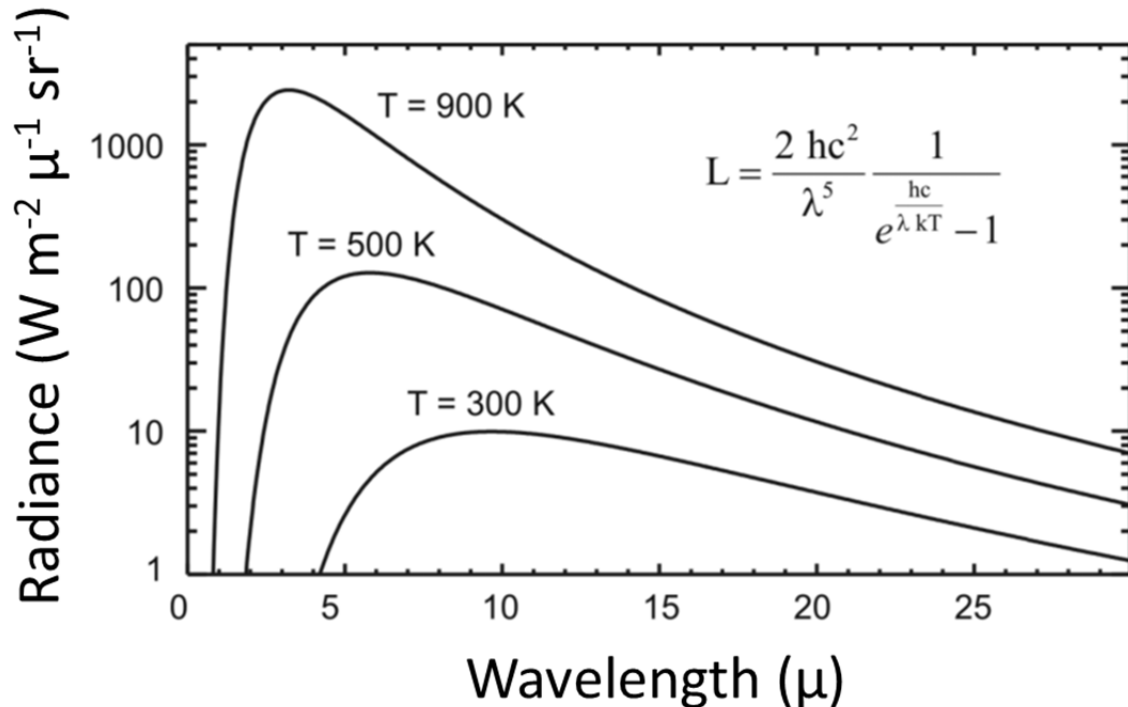
Figure 4.   Blackbody radiation as a function of wavelength. After Olsen (2007)

Planck's law calculates energy as radiance in

$$Radiance = L = \frac{2hc^2}{\lambda^5} \frac{1}{e^{\frac{hc}{\lambda kT}} - 1},$$ (9)

where c is the speed of light in a vacuum, h is the Planck constant, k is the Boltzmann constant, T is temperature, and λ is wavelength (Olsen 2007).

The solar spectrum is not continuous as would be expected if the sun was a blackbody. Rather the solar irradiance curve follows the blackbody curve, but is not smooth like the blackbody curve shown in Figure 5.
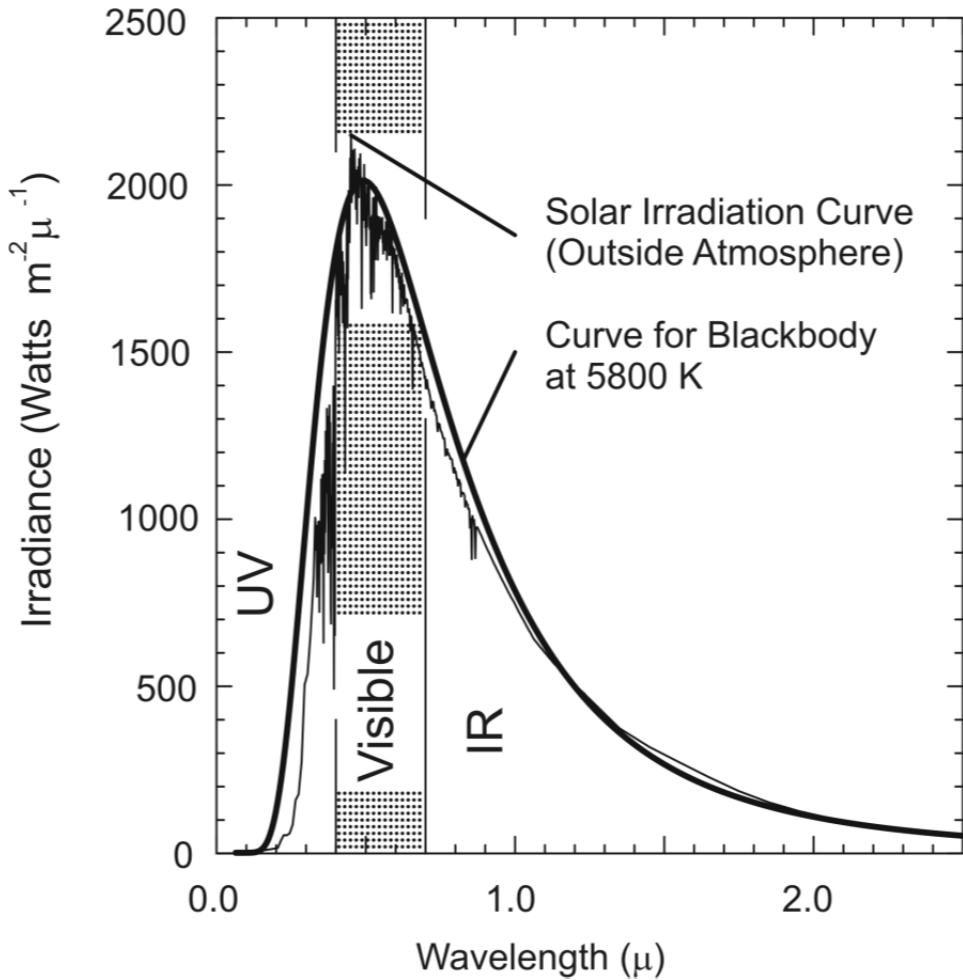
Figure 5.   The solar spectrum. From Phillips (1995)

This is due to solar absorption features. Solar absorption features are gases above the sun's surface that contain atoms or molecules that absorb photons of certain wavelengths. These create absorption lines in the solar spectrum called Frauenhofer Lines. The Frauenhofer Line at 760 nm is caused by oxygen and is particularly important to one of the sun glint correction methods tested in this thesis.

Some of the most prominent absorption features seen in imaging spectrometry are from water vapor and carbon dioxide in Earth's atmosphere. Figure 6 illustrates how the transmittance of photons through Earth's atmosphere changes as a function of wavelength.
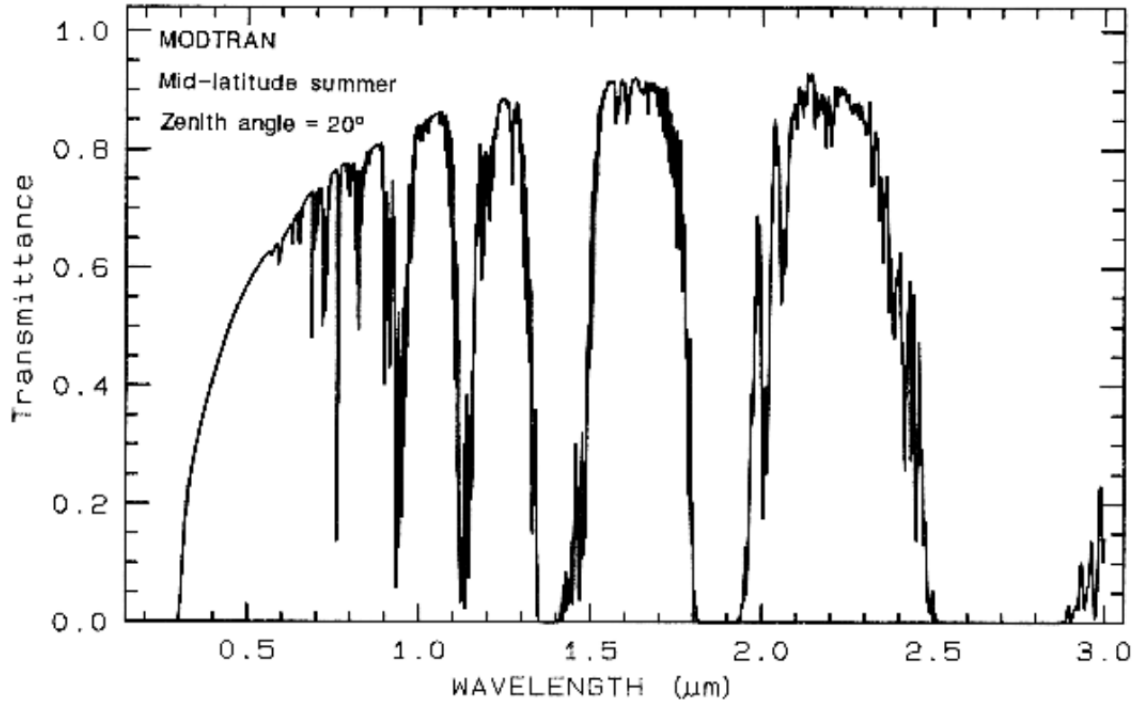
Figure 6.   MODTRAN modeled atmospheric transmittance in the VNIR and SWIR wavelengths. From Berk et al. (1989)

Clark (1999) describes these changes in transmittance as atmospheric "windows" for remote sensing. Major water vapor absorption features for the VNIR and SWIR wavelengths are located approximately at 900, 1100, 1400, and 1900 nm. Major carbon dioxide absorption features for the VNIR and SWIR wavelengths are located at approximately 2010 and 2080 nm (Van Der Meer and De Jong 2006). To derive physical

parameters such as reflectance from imaging spectrometry, atmospheric correction must be applied to imagery. Many atmospheric correction methods are based on the MODerate resolution atmospheric TRANsmission (MODTRAN) model with the Tafkaa method showing promise for littoral zone remote sensing (Montes et al. 2004). The test image used in this thesis is not atmospherically corrected to determine the true effect of sun glint correction algorithms on unmodified pixel values.

8. Radiative Transfer

Radiative transfer theory helps to model EMR flow from the sun to an optical remote sensing detector above Earth's surface. Radiative transfer models are useful to understanding the interaction of EMR with features on earth and how that interaction manifests itself in remotely sensed imagery. Bukata et al. (1995) provides a good introduction to radiative transfer theory. Hochberg et al. (2003) provides a useful radiative transfer model for modeling sun glint and for developing sun glint correction algorithms. A sensor's measurement of total upwelling radiance $L_{TOT}(\lambda)$ at wavelength λ includes contributions from the atmosphere $L_{atm}(\lambda)$, water surface $L_g(\lambda)$, and water column $L_w(\lambda)$ in

$$L_{TOT}(\lambda) = L_{atm}(\lambda) + T(\lambda) \times L_g(\lambda) + T(\lambda) \times L_w(\lambda), \tag{10}$$

where atmospheric transmittance is $T(\lambda)$ (Hochberg et al. 2003). Equation (10) can be expanded for image data by including the spatial distribution function $f_x(x, y; \lambda)$ for each of the radiance terms. The spatial distribution functions are relative scaling factors for each pixel and wavelength $(x, y; \lambda)$, while absolute magnitudes are provided by the radiances $L_x(\lambda)$. Sun glint can be modeled in image data with the spatial distribution function $f_g(x, y)$. The spatial distribution function $f_w(x, y)$ can model the subsurface features in image data including features from the water column and the sea floor in

$$
\begin{aligned}
f_{TOT}(x, y; \lambda) &\times L_{TOT}(\lambda) = \\
f_{atm}(x, y; \lambda) &\times L_{atm}(\lambda) + T(\lambda) \times f_g(x, y; \lambda) \times L_g(\lambda) + T(\lambda) \times f_w(x, y; \lambda) \times L_w(\lambda).
\end{aligned}
\tag{11}
$$

15

If atmospheric correction is applied to an image, $f_{atm}(x,y;\lambda) \times L_{atm}(\lambda)$ is removed and Equation (11) becomes

$$[f_{TOT}(x,y;\lambda) \times L_{TOT}(\lambda)]' = f_g(x,y;\lambda) \times L_g(\lambda) + f_w(x,y;\lambda) \times L_w(\lambda). \qquad (12)$$

The goal of sun glint correction methods is to calculate and remove $f_g(x,y;\lambda) \times L_g(\lambda)$ and produce the desired water leaving radiance image $f_w(x,y;\lambda) \times L_w(\lambda)$ (Hochberg et al. 2003).

B.   SUN GLINT

1.   Sun Glint Geometry

Mobley (1994) defines geometrical radiometry as the union of euclidean geometry and radiometry. Sun glint geometry can be modeled using geometrical radiometry and is summarized by three components consisting of the sun angle, sensor viewing angle, and surface orientation. Sun angle and sensor viewing angle are typically measured from zenith where the sun angle is θ_I, sensor viewing angle is θ_F, and I, R, and Z are the incidence, reflection, and zenith vectors, respectively, in Figure 7.   The zenith vector is a straight line drawn from the center of earth to the sun in a direction opposite of gravity. Sun glint occurs when the sun angle is equal to the sensor viewing angle with respect to the surface normal vector n in Figure 7. For sun glint to occur, the incidence, reflection, and surface normal vectors must lie in the same plane (Kay et al. 2009). In specular reflection from a flat water surface, the surface normal vector is equivalent to the zenith vector and the sun angle and sensor viewing angle are equal to angle ω in Figure 7. In rough water, the surface normal vector is not equivalent to the zenith vector and the sun and sensor viewing angles are not equal to angle ω.
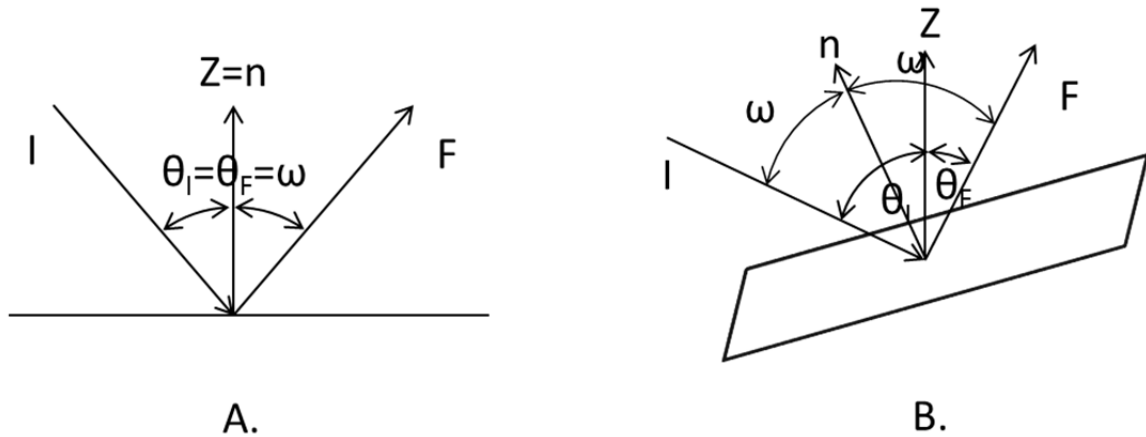
Figure 7. Sun glint geometry of a smooth surface (A.) and a rough surface (B.).
After Kay et al. (2009) and Mobley (1994)

Sun glint in remotely sensed imagery occurs in two forms; cross-track and wave-induced. Cross track glint occurs when the sun angle is such that sun glint manifests itself perpendicular to the motion of the sensor usually leaving half of the image with high intensity sun glint and the other half with very little sun glint. Wave-induced sun glint occurs when the surface orientation component of sun glint geometry introduces reflections off of wave facets. Sky glint is the reflection of atmospherically scattered light off of the wave facets of the sea surface (Kay et al. 2009). Both sky glint and wave-induced sun glint can create ocean surface clutter obscuring features in the water. Figure 8 depicts a sea surface model and wave facets positioned in different orientations.
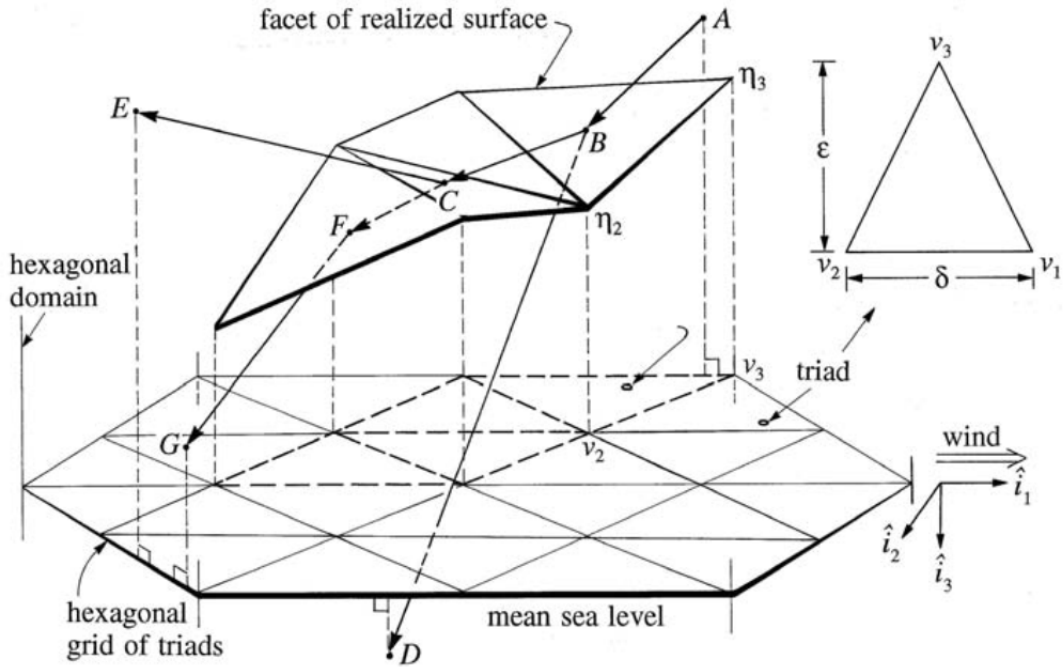
Figure 8.   Model of the sea surface with triangular wave facets. From Mobley (1994)

Sky glint can be more of a factor than sun glint in some images that contain wave-induced ocean surface clutter. Sun glint correction methods may not minimize sky glint resulting in the need for different methods to reduce ocean surface clutter (Silva and Abileah 1999). This thesis deals specifically with cross track sun glint and does not address sky glint.

2.   Sun Glint Avoidance

Sun glint is strictly a geometric problem. Therefore, careful flight planning can increase the likelihood of sun glint-free imagery. The position of the sun near solar zenith and during seasons of high inclination can increase the potential of creating sun glint in imagery. Some imaging systems attempt to avoid sun glint in their images by employing tilting sensors that alter the viewing angle of the sensor with respect to the location of the sun. Tilting sensors are typically deployed on satellite platforms where

the sun's position relative to the sensor can be calculated. The Compact High Resolution Imaging Spectrometer sensor utilizes a multi-look angle image collection method to eliminate sun glint (Van Mol and Ruddick 2004). In situations where sun glint is unavoidable and appears in imagery, sun glint correction algorithms can be used to minimize its effects.

3. Sun Glint Correction in Low Spatial Resolution Imagery

Remote sensing imaging systems used to study ocean color typically have spatial resolutions on order of hundreds of meters or kilometers. Included in this category are the Sea-viewing Wide Field-of-view Sensor, the Medium Resolution Imaging Spectrometer, and the Global Imaging Sensor (Wang and Bailey 2001) (Ottaviani et al. 2008) (Montagner et al. 2003) (Fukushima et al. 2007). When sun glint occurs in images from these types of sensors, the sun glint may cover hundreds of meters of ocean. Most sun glint correction algorithms developed for low spatial resolution sensors are based on work from Cox and Munk (1954). Cox and Munk (1954) used statistical analysis to create probability distribution functions for sea surface state by measuring aerial photographs and wind-speed. While the Cox and Munk (1954) method may work well for low spatial resolution imagery, it is not suitable for high spatial resolution imagery where the imagery is at the wave face scale opposed to the sea surface scale.

4. Sun Glint Correction in High Spatial Resolution Imagery: Methods Comparison

a. *Silva and Abileah*

Sun glint in high spatial resolution imagery can be removed with sun glint correction methods that exploit the high absorption of water in the Near Infrared (NIR) wavelengths. Silva and Abileah (1999) provide a radiative transfer model where $L_u(\lambda)$ is upwelling radiance, $L_b(\lambda)$ is backscattered and reflected radiance from the sky, and $f_b(x, y)$ is the spatial distribution function for the backscattered and reflected radiance from the sky in

$$[f_{TOT}(x, y; \lambda) \times L_{TOT}(\lambda)]' = L_u(\lambda) + f_b(x, y; \lambda) \times L_b(\lambda) + f_g(x, y; \lambda) \times L_g(\lambda). \quad (13)$$

19

Upwelling radiance is combined with the backscattered and reflected radiance from the sky due to the difficulty of separating the two contributions to create the scattered radiance term $f_s(x,y) \times L_s(\lambda)$ in

$$[f_{TOT}(x,y;\lambda) \times L_{TOT}(\lambda)]' = f_s(x,y;\lambda) \times L_s(\lambda) + f_g(x,y;\lambda) \times L_g(\lambda). \qquad (14)$$

$L_g(\lambda)$ and $L_s(\lambda)$ are obtained from the top and bottom one to five percent of the brightest and darkest pixels, respectively. The $f_g(x,y)$ and $f_s(x,y)$ terms are obtained from a least squares regression and combined with $L_g(\lambda)$ and $L_s(\lambda)$ to estimate sun glint. The sun glint estimate is then subtracted from the input image resulting in an image free of sun glint.

b.   Mustard et al.

Mustard et al. (2001) identified the magnitude of the sun glint contribution in the NIR band where $f_w(x,y;NIR) \times L_w(NIR)$ should effectively be 0. Pixels of NIR bands that show no reflectance of objects on the surface or returns from the seafloor and are said to be optically deep. Equation (12) reduces to

$$[f_{TOT}(x,y;NIR) \times L_{TOT}(NIR)]' = f_g(x,y;NIR) \times L_g(NIR). \qquad (15)$$

All aquatic NIR images are the product of the spatially relative glint intensity weighted by the absolute glint intensity. Absolute glint intensity varies across wavelengths. Because water reflectance has a weak dependence on wavelength (Mobley 1994), relative glint intensity in the VIS wavelengths varies accordingly with the relative glint intensity in the NIR wavelengths, as shown in

$$f_g(x,y;VIS) = f_g(x,y;NIR) = f_g(x,y). \qquad (16)$$

c.   Hochberg et al.

Hochberg et al. (2003) created an algorithm that finds the brightest (i,j) and the darkest (i',j') NIR pixels in an image and subtracts them to obtain $L_g(NIR)$ using

20

$$L_g(NIR) = f_g(i,j;NIR) \times L_g(NIR) - f_g(i',j';NIR) \times L_g(NIR) =$$
$$[L_g(NIR) + L_w(NIR)] - L_w(NIR). \tag{17}$$

The absolute magnitude of water leaving radiance in the NIR bands $L_w(NIR)$ should be 0 due to the absorption of water in the NIR wavelengths. Hochberg et al. (2003) found that residual radiance nearly always made $L_w(NIR)$ positive. Scaling the NIR image to be between 0 and 1 is accomplished by

$$f_g(x,y) = \frac{[f_{TOT}(x,y;NIR) \times L_{TOT}(NIR)]' - L_w(NIR)}{L_g(NIR)}. \tag{18}$$

Equation (17) is repeated with the VIS bands substituted for the NIR band such that

$$L_g(VIS) = f_g(i,j;VIS) \times L_g(VIS) - f_g(i',j';VIS) \times L_g(VIS) =$$
$$[L_g(VIS) + L_w(VIS)] - L_w(VIS). \tag{19}$$

The product of Equations (18) and (19) is subtracted from $[f_{TOT}(x,y;VIS) \times L_{TOT}(VIS)]'$ to obtain the VIS bands with the glint removed, as shown in

$$f_w(x,y;VIS) \times L_w(VIS) = [f_{TOT}(x,y;VIS) \times L_{TOT}(VIS)]' - f_g(x,y) \times L_g(VIS). \tag{20}$$

d.   Hedley et al.

The weakness of the Hochberg et al. (2003) sun glint correction method is that a linear relationship between the brightest (i,j) and the darkest (i',j') NIR pixels is established with only two pixels. As a result, this method is sensitive to outliers and requires masking all land and cloud pixels prior to analysis. Hedley et al. (2005) improved upon the method by establishing a linear relationship between the NIR and VIS bands using linear regression based on a range of optically deep water pixels affected by sun glint that would otherwise have consistent spectral brightness as shown in Figure 9.
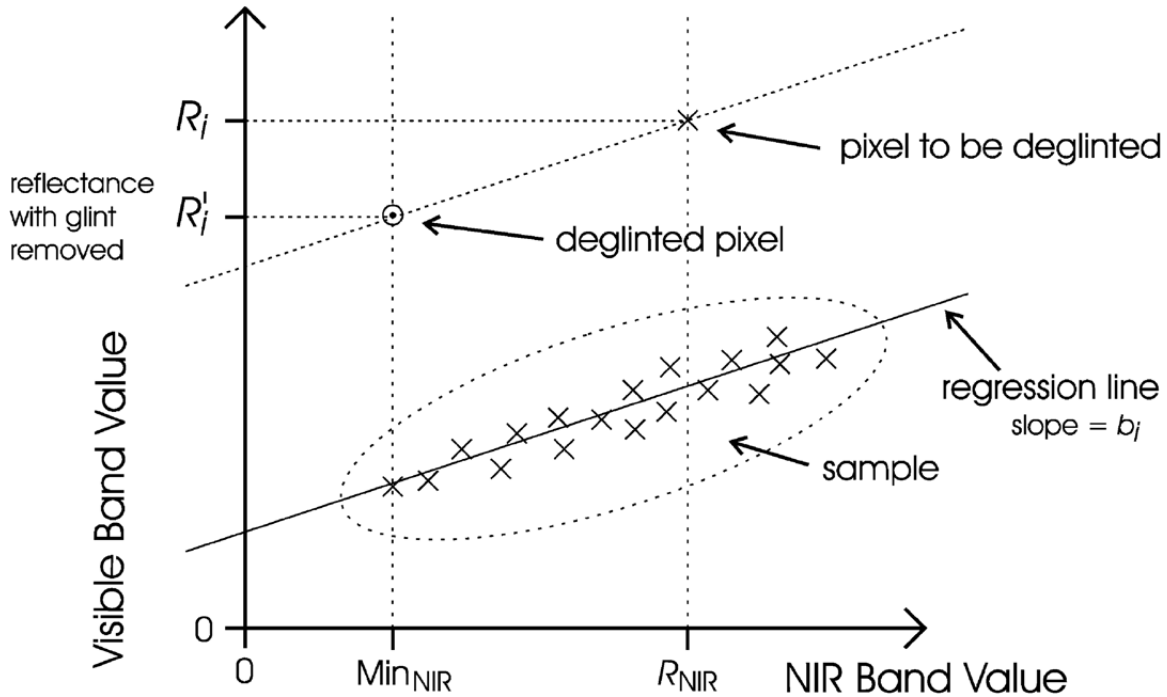
Figure 9.   Graphical interpretation of the Hedley et al. (2005) sun glint correction
method. From Hedley et al. (2005)

First, a sample of deep water pixels with a variety of glint intensities is chosen and the
minimum NIR brightness Min_{NIR} of the sample is calculated. To remove glint in each
VIS band i, a linear regression is performed on the NIR pixel brightness R_{NIR} against the
pixel value of VIS band R_i. The product of slope b_i and R_{NIR} minus Min_{NIR} is
subtracted from R_i to obtain the pixel R_i' with glint removed such that

$$R_i' = R_i - b_i \times (R_{NIR} - Min_{NIR}).$$ \hfill (21)

Because the sample selection is user-based, there is no need to mask land and cloud
pixels. Linear regression makes the method robust to outliers caused by non-optically
deep pixels.

22

e. *Lyzenga et al.*

A slightly different approach to the Hedley et al. (2005) sun glint correction method involves computing the covariance of each VIS band relative to the NIR band (Lyzenga et al. 2006). Similar to the Hedley et al. (2005) method, a user defines a sample area of varying glint intensities over deep water. Instead of using linear regression to calculate the coefficient that relates the NIR sun glint signal to the VIS band, Lyzenga et al. (2006) uses the equation

$$\rho_{ij} \;=\; \frac{1}{N}\sum_{n=1}^{N} L_{in}L_{jn} \;-\; \frac{1}{N}\sum_{n=1}^{N} L_{in}\,\frac{1}{N}\sum_{n=1}^{N} L_{jn} \tag{22}$$

to calculate the covariance between the VIS (*i*) and NIR (*j*) bands ρ_{ij}. The covariance is divided by the variance of the NIR band

$$r_{ij} = \frac{\rho_{ij}}{\rho_{jj}} \tag{23}$$

to obtain the coefficient r_{ij}. The correction is applied using a modification of Equation (21)

$$R_i' = R_i - r_{ij} \times (R_{NIR} - Mean_{NIR}), \tag{24}$$

using the mean NIR radiance used rather than the minimum. The modal NIR radiance can also be used (Joyce 2004).

f. *Goodman et al.*

The residual radiance in the NIR waveband found by Hochberg et al. (2003) can result in both over and under corrected spectral outputs in the VIS bands when applied to imagery containing cross-track sun glint (Goodman et al. 2008). The Hochberg et al. (2003) method can be successful at correcting wave-induced sun glint because only one correction relationship is applied to the entire image. In the case of cross-track sun glint, a more dynamic approach is needed to correct for a greater variety of sun glint intensities. Goodman et al. (2008) found that performing corrections independently on each pixel was more effective at removing cross-track sun glint. A

23

method derived from Lee et al. (1999) was used where sun glint correction was applied as a constant offset across all wavelengths such that reflectance at 750 nm R_{750} is equal to a spectral constant Δ in

$$R_i' = R_i - R_{750} + \Delta .\tag{25}$$

The spectral constant offset is calculated using the product of two summed constants and the difference between the reflectance values at 640 nm and 750 nm, as in

$$\Delta = 0.000019 + 0.1[R_{640} - R_{750}].\tag{26}$$

The constant values force the reflectance at 750 nm to approach zero, but allow it to be a little above zero for shallow water. The values provided by Goodman et al. (2008) are for Airborne Visible/Infrared Imaging Spectrometer (AVIRIS) data and would need to be adjusted for other sensors by optimizing with in situ data.

g.   *Kuster et al.*

Kuster et al. (2009) suggests the amount of glint is proportional to the depth of the 760 nm oxygen absorption feature D in

$$D = \frac{R(739) + R(860)}{2} - R(760) ,\tag{27}$$

where $R(\lambda)$ is the reflectance in the 739, 760, and 860 nm bands, respectively. The 739 and 860 nm bands are outside of the 760 nm oxygen absorption feature and D represents the reflectance without oxygen present. The D value at a certain pixel (x, y) is divided by the maximum D value found in a deep water region in

$$D_{norm}(x, y) = \frac{D(x, y)}{D_{max}}\tag{28}$$

to obtain the normalized $D_{norm}(x, y)$ value of a pixel. If D is zero, then it follows that the pixel has no glint. The spectral variation of glint $G(\lambda)$ is calculated by subtracting the NIR band with the lowest D value from the NIR band with the highest in

$$G(\lambda) = R_{bright}(\lambda) - R_{dark}(\lambda).\tag{29}$$

The product of $G(\lambda)$ and $D_{norm}(x, y)$ gives the amount of glint in each band at each pixel. The glint is then subtracted from the reflectance of each pixel in each band $R(x, y; \lambda)$ in

$$R_w(x, y; \lambda) = R(x, y; \lambda) - G(\lambda) \times D_{norm}(x, y), \qquad (30)$$

where $R_w(x, y; \lambda)$ is the glint corrected pixel. This method requires the high spectral resolution of hyperspectral imagery with bands very close to 760 nm to determine the oxygen absorption feature.

THIS PAGE INTENTIONALLY LEFT BLANK

III.   DATA AND METHODOLOGY

A.   DATA

The hyperspectral image used for this thesis is from an airborne survey near San Diego, California performed by SpecTIR Inc. on March 20, 2012, under contract by United Technologies (UTC) Aerospace Systems (formerly Goodrich Inc.).   The test image used is one of seven flight lines covering coastal waters off of La Jolla, California originating off-shore and extending on-shore.   The imaging system used was a ProSpecTIR-VS3 dual sensor bracket mount combining Airborne Imaging Spectrometer for Applications (AISA) Eagle and Hawk sensors into a single imaging system (SpecTIR 2011).   The AISA Eagle is a VNIR sensor with a wavelength range of approximately 400–970 nm and the AISA Hawk sensor is a SWIR sensor with a wavelength range of approximately 970–2,450 nm.   The integrated imaging system has 360 bands with a spectral range of approximately 400 to 2,450 nm and a swath width of 320 pixels.   The full extent of the test image is 320 by 3,528 pixels in BIL format.   Radiometric and spectral calibration was performed on the test image by SpecTIR, but no atmospheric correction was applied.   Figure 10 provides the actual FWHM band passes of the 5 nm nominal spectral resolution.
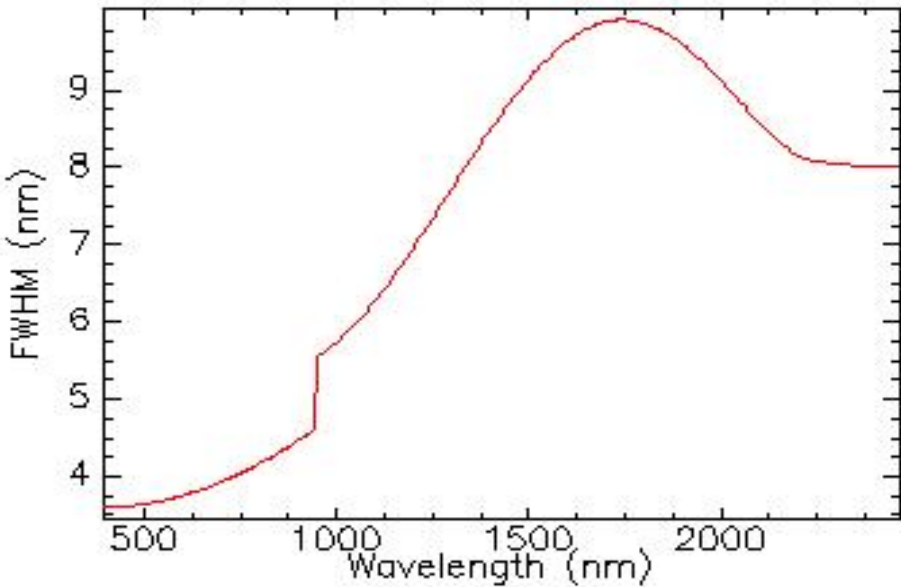
Figure 10.   Graph of FWHM band passes by wavelength for the ProSpecTIR-VS3 imaging system.

The survey was flown mid-day to induce sun glint at an altitude that provided one meter GSD.   The data are stored as 16-bit unsigned integers in calibrated radiance units ($mW\ cm^{-2}\ sr^{-1}\ \mu m^{-1}$) with a scaling factor of 1,000.   Figure 11 illustrates that the image has a strong gradient of cross-track sun glint affecting the right half of the image.   The red line across the width of the image in Figure 11 is a Region of Interest (ROI) drawn over optically deep water with no surface features.   The deep water ROI is the 3,000[th] row of the image representing all 320 pixel columns across the scan width.

Figure 11.   True-color composite depiction of the hyperspectral test image with cross
track sun glint. Blue represents the (456–464 nm) band, green represents the
(548–555 nm) band, and red represents the (637–645 nm) band. The red line
represents the deep water ROI pixel locations of (1-320, 3000).

Figure 12 provides pixel radiance values of four VNIR bands from the test image
plotted against the position of the pixel along the deep water ROI. The four VNIR bands
plotted in the graph include blue (456–464 nm), green (548–555 nm), red (637–645 nm),
and NIR (856–865 nm).   The spatial profiles show progressively greater radiance
variance from left to right in the image due to sun glint. The dashed lines show the
strong positive slope of the spatial profiles that, in the absence of sun glint, should be
nearly horizontal due to the homogeneity of the deep water ROI.
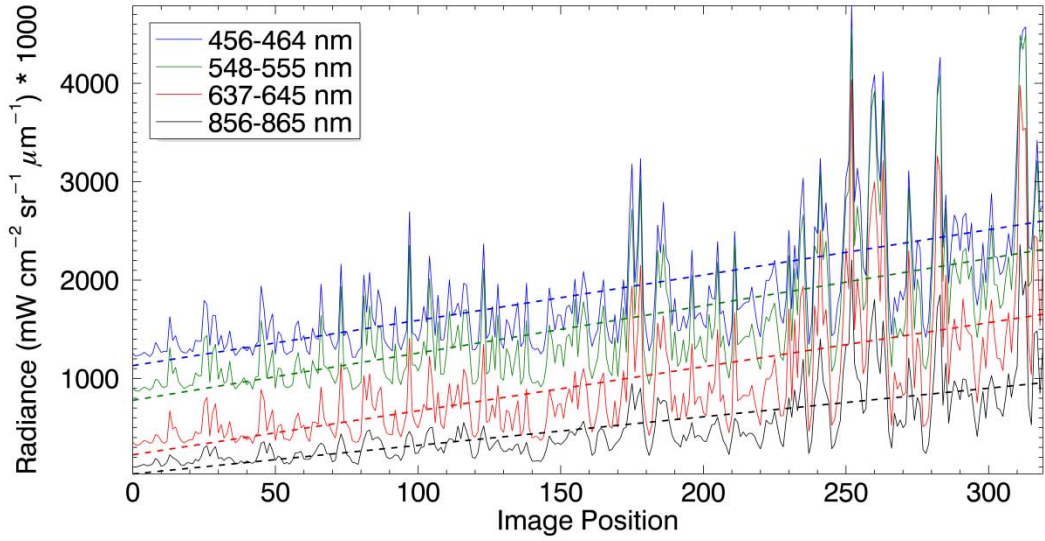
Figure 12.   Spatial profile of four VNIR bands from the test image at the deep water
ROI pixel locations of (1-320, 3000).

Table 1 presents the summary statistics for the four VNIR bands in Figure 12. Standard deviation values are large and correlation values are low illustrating sun glint effect on the image. Slope values are large and positive corresponding to the strong positive slope lines in Figure 12. In the absence of sun glint, the slope values should be close to zero. The NIR band is less affected by sun glint compared to the VIS bands owing to the NIR absorptive property of water.

Table 1.   Summary statistics of four VNIR bands from the test image at the deep water
ROI pixel locations of (1-320, 3000).

Band			Test Image						
	Wavelength (nm)		Radiance (mW cm^{-2} sr^{-1} μm^{-1}) * 1000						
Color	Peak	Range	Max	Min	Mean	Median	Mode	Standard Deviation	Slope
Blue	460	456-464	4788	1214	1865.360	1650	1387	657.539	4.60288
Green	552	548-555	4563	870	1544.580	1342	1004	694.227	4.80715
Red	641	637-645	4035	323	938.588	750	621	640.973	4.47657
NIR	860	856-865	2364	99	493.541	375	362	378.298	2.90338

The spectral plot in Figure 13 depicts spectra from pixel (1, 3000) at the far left end of the test image deep water ROI and pixel (320, 3000) at the far right end of the test image deep water ROI. Note the large discrepancy in radiance between the two spectra and the correlation value of 0.86. It is expected that, in the absence of sun glint, these two spectra should be closer together and have a higher correlation value because they are from the same deep water ROI.
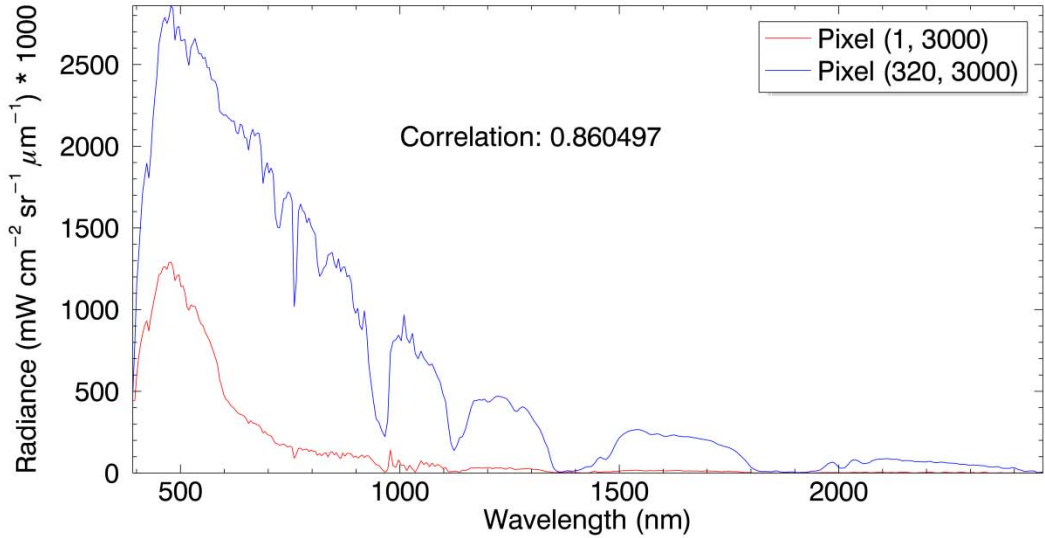
Figure 13.   Spectral plot of radiance by wavelength for a pixel with a low amount of sun glint at the deep water ROI location of (1, 3000) (red) and a pixel with a high amount of sun glint at the deep water ROI location of (320, 3000) (blue) of the test image.

B.   METHODOLOGY

The sun glint correction methods of Hedley et al. (2005), Lyzenga et al. (2006), Joyce (2004), and Kuster et al. (2009) were written as algorithms within the Interactive Data Language (IDL) 8.0 workbench environment using ENvironment for Visualizing Images (ENVI) library routines (see Appendices A–D). The IDL sun glint correction algorithms were applied to all 360 bands of the test image and the corrected images were visually compared. The Hedley et al. (2005), Lyzenga et al. (2006), and Joyce (2004)

methods are fundamentally similar and can be categorized as the regression-based methods. The deep water ROI and 856–865 nm NIR band were used for the regression-based sun glint correction algorithms.

Spatial profiles were created for the deep water ROI pixels in the sun glint corrected images using the four VNIR bands as shown in Figure 12. The spatial profiles were visually compared to the test image and the other sun glint corrected images to obtain a qualitative assessment of the sun glint correction algorithms performance in the VNIR region. Summary statistics of the spatial profiles for all 360 bands in each image were calculated. Slope values for each image were plotted by band and compared to the test image slope values. The slope plots determined which bands were under-corrected or over-corrected. Slope values closer to zero performed better, while positive slope values represented under-correction and negative slope values represented over-correction.

Spectral plots for the deep water ROI pixel with a low amount of sun glint at (1, 3000) and the deep water ROI pixel with a high amount of sun glint at (320, 3000) in the sun glint corrected images were created. For each sun glint corrected image, the spectral plots were compared and correlation values were calculated to determine how well the low and high sun glint spectra matched each other after correction. The corrected spectra were also compared to the original spectra and correlation values were calculated to evaluate how well the corrected spectra maintained spectral integrity. Correlation values were averaged for each sun glint correction method and the algorithm that resulted in the highest average correlation was designated as the best performing with respect to spectral fidelity.

IV. RESULTS AND DISCUSSION

A. RESULTS AND DISCUSSION

1. Visual Comparison

Figure 14 illustrates the results of the four sun glint correction algorithms compared to the uncorrected test image. The three regression-based algorithms performed similarly at correcting glint from the test image compared to the Kuster et al. algorithm. The similar results from the regression-based methods are expected given that the only real difference between them is the deep water ROI NIR statistic used in the algorithm. The Hedley et al. method uses the minimum deep water ROI NIR value, while the Lyzenga et al. method uses the mean deep water ROI NIR value and the Joyce method uses the modal deep water ROI NIR value. The Kuster et al. method uses an entirely different algorithm based on the 760 nm oxygen absorption feature. Some sun glint remains in the resulting image from the Kuster et al. algorithm. All four of the sun glint correction algorithms resulted in black land pixels, essentially making these pixels unusable for spectral analysis.

(A.)	(B.)	(C.)	(D.)	(E.)
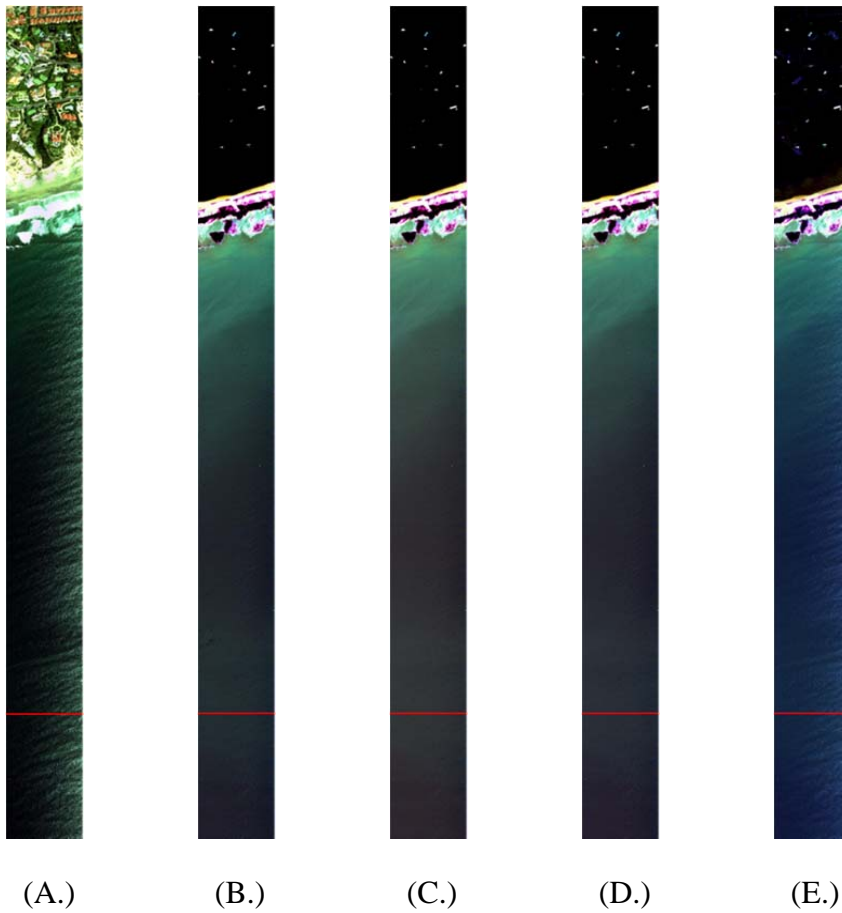
Figure 14.   True-color composite depictions of the hyperspectral test image (A.), and sun glint corrected images from the methods of Hedley et al. (B.), Lyzenga et al. (C.), Joyce (D.), and Kuster et al. (E.). Blue represents the (456–464 nm) band, green represents the (548–555 nm) band, and red represents the (637–645 nm) band. The red lines represent the deep water ROI pixel locations of (1–320, 3000).

2.   Spatial and Spectral Methods Comparison

a.   Hedley et al.

Figure 15 provides spatial profiles of four VNIR bands from the Hedley et al. sun glint corrected image at the deep water ROI pixel locations of (1-320, 3000). The radiance variances on the right side of the profiles are smoothed compared to the test image profiles in Figure 12. The dashed lines of the RGB spatial profiles depict a weak

negative slope while the dashed line of the NIR spatial profile depicts a flat slope. The NIR spatial profile intersects the y-axis at the minimum deep water ROI NIR value used in the algorithm.
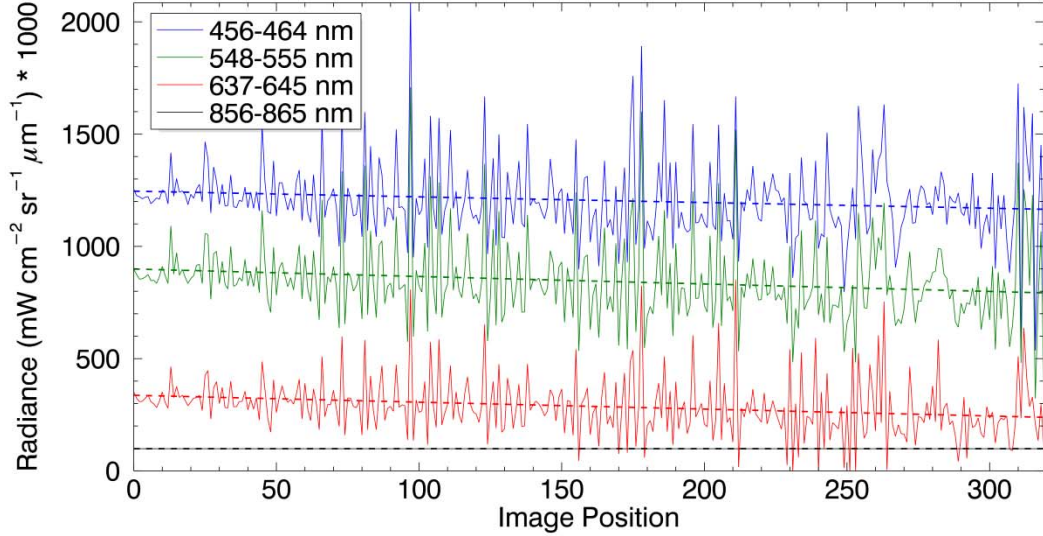
Figure 15.   Spatial profile of four VNIR bands from the Hedley et al. sun glint corrected image at the deep water ROI pixel locations of (1-320, 3000).

Table 2 details the summary statistics for the four VNIR bands in Figure 15. The shaded cell represents the deep water ROI NIR value used in the Hedley et al. sun glint correction algorithm. Standard deviation values are smaller and slope values are closer to zero than the test image statistics in Table 1. The slope values for the VIS bands are negative depicting that the algorithm over-corrected for sun glint in these bands. The zero values for standard deviation and slope in the NIR band exemplifies that the NIR band used in the algorithm was applied to itself setting the profile to the minimum deep water ROI radiance value of this band.

Table 2.   Summary statistics of four VNIR bands from the Hedley et al. sun glint corrected image at the deep water ROI pixel locations of (1-320, 3000). The highlighted cell depicts the minimum NIR value used in the Hedley et al. sun glint correction algorithm.

Band			Hedley et al. Sun Glint Corrected Image						
	Wavelength (nm)		Radiance (mW cm^{-2} sr^{-1} μm^{-1}) * 1000						
Color	Peak	Range	Max	Min	Mean	Median	Mode	Standard Deviation	Slope
Blue	460	456-464	2085	536	1205.550	1189	1172	179.251	-0.253
Green	552	548-555	1709	323	846.097	824	835	182.857	-0.333
Red	641	637-645	852	0	287.853	282	286	135.679	-0.308
NIR	860	856-865	99	99	99.000	99	99	0.000	0.000

Figure 16 characterizes the slope values plotted by wavelength for all bands of the uncorrected test image and the Hedley et al. sun glint corrected image. The negative corrected slope values show that the Hedley et al. sun glint correction algorithm over-corrected for sun glint in most of the VNIR bands.
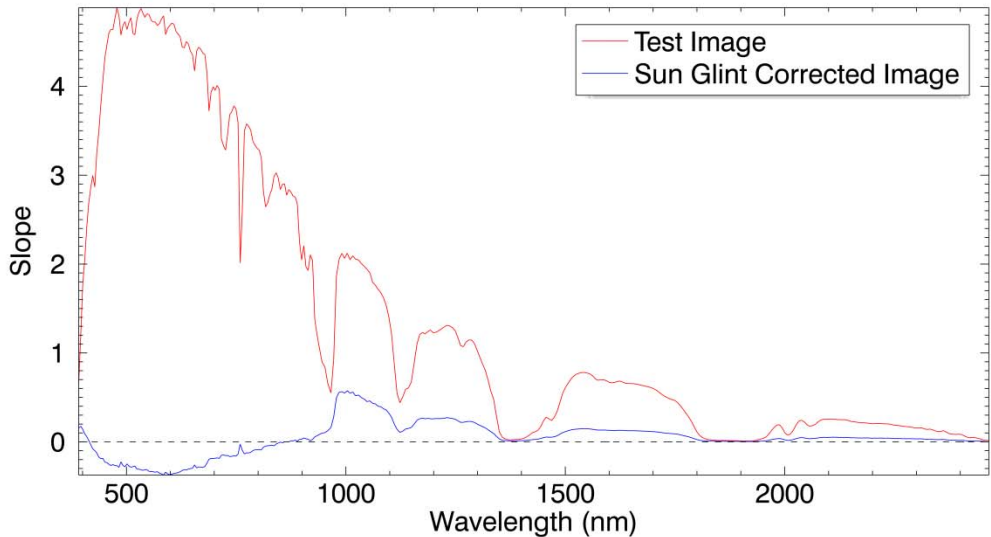
Figure 16.   Plot of slope by wavelength for the uncorrected test image (red) and the Hedley et al. sun glint corrected image (blue).

Figure 17 presents spectra from a deep water ROI pixel with a low amount of sun glint at (1, 3000) and a deep water ROI pixel with a high amount of sun glint at

(320, 3000) for the Hedley et al. sun glint corrected image. The algorithm over-corrected the radiance of the pixel with the high amount of sun glint to less than the pixel with the low amount of sun glint in the VNIR bands.
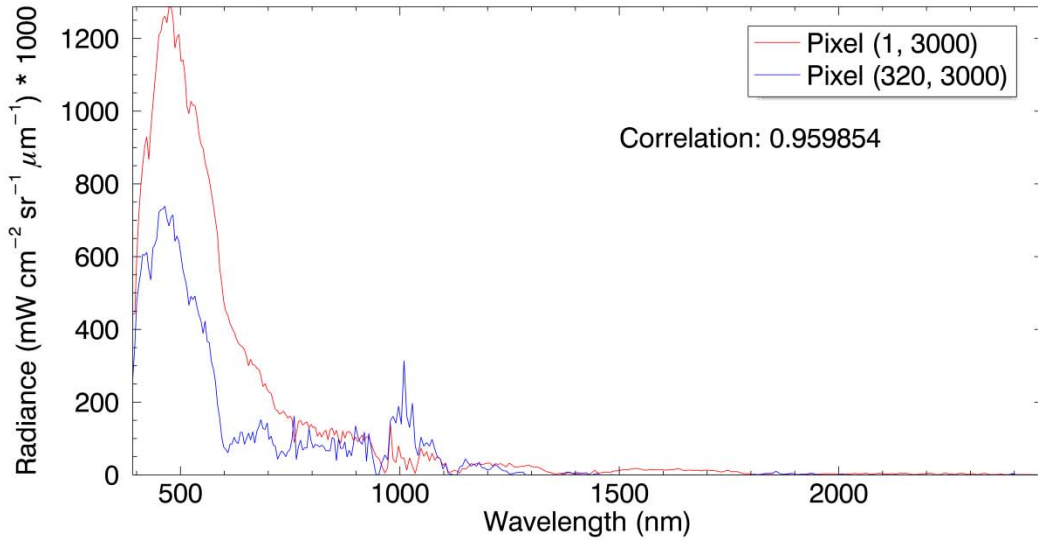
Figure 17.   Spectral plot of radiance by wavelength for a pixel with a low amount of sun glint at the deep water ROI location of (1, 3000) (red) and a pixel with a high amount of sun glint at the deep water ROI location of (320, 3000) (blue) of the Hedley et al. sun glint corrected image.

Figure 18 depicts spectra from a pixel with a low amount of sun glint from the deep water ROI pixel at (1, 3000) of the uncorrected test image and the same pixel in the Hedley et al. sun glint corrected image. The algorithm did not significantly alter the spectrum of the pixel from the test image as represented by the high correlation value.

37
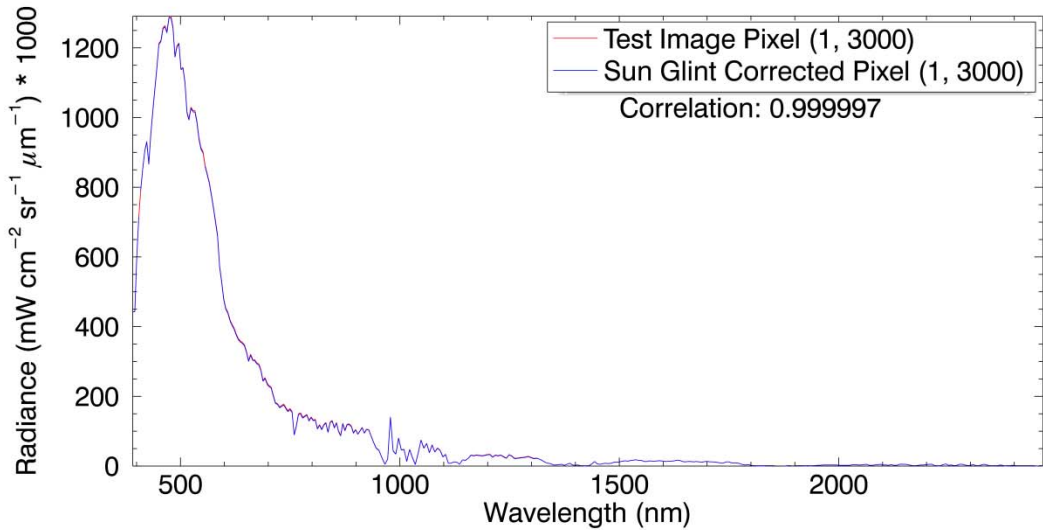
Figure 18. Spectral plot of radiance by wavelength for a pixel with a low amount of sun glint at the deep water ROI location of (1, 3000) (red) of the test image and a pixel with a low amount of sun glint at the deep water ROI location of (1, 3000) (blue) of the Hedley et al. sun glint corrected image.

Figure 19 shows spectra from a pixel with a high amount of sun glint from the deep water ROI pixel at (320, 3000) of the test image and the same pixel in the Hedley et al. sun glint corrected image. The algorithm vastly altered the spectrum shape of the pixel in the VNIR bands making the spectrum unrecognizable from the original spectrum as represented with the low correlation value. Many of the VNIR spectral features in the original spectrum were lost and the 760 nm oxygen absorption feature was inverted into a slight peak in the corrected spectrum. Spectral features in the SWIR region beginning at the water absorption feature at 900 nm in the corrected spectrum are consistent with the original spectrum.
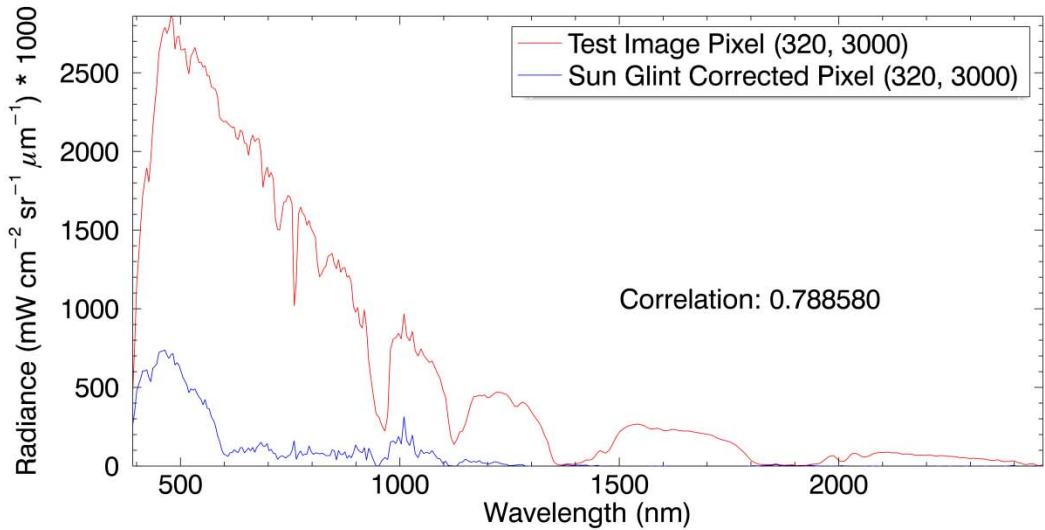
Figure 19.   Spectral plot of radiance by wavelength for a pixel with a high amount of
sun glint at the deep water ROI location of (320, 3000) (red) of the test image
and a pixel with a high amount of sun glint at the deep water ROI location of
(320, 3000) (blue) of the Hedley et al. sun glint corrected image.

b.   *Lyzenga et al.*

Figure 20 displays spatial profiles of four VNIR bands from the Lyzenga
et al. sun glint corrected image for deep water ROI pixel locations of (1-320, 3000). The
radiance variances on the right side of the profiles are smoother compared to the test
image profiles in Figure 12. The dashed lines of the RGB profiles show a weak negative
slope and the dashed line of the NIR profile shows a flat slope.   The NIR profile
intersects the y-axis at the mean deep water ROI NIR value used in the algorithm.
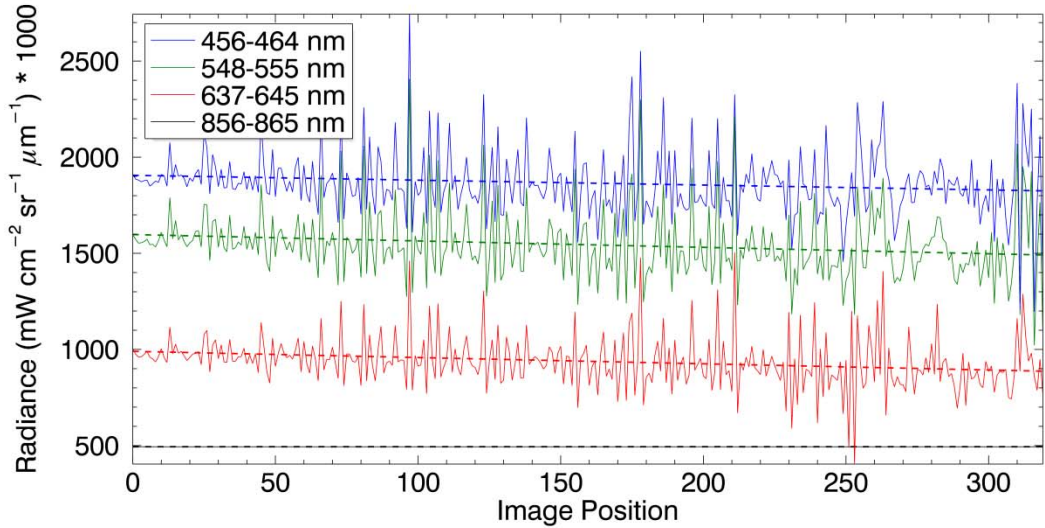
Figure 20.   Spatial profile of four VNIR bands from the Lyzenga et al. sun glint corrected
image at the deep water ROI pixel locations of (1-320, 3000).

Table 3 provides summary statistics for the four VNIR bands in Figure 20. The shaded cell represents the deep water ROI NIR value used in the Lyzenga et al. sun glint correction algorithm. Standard deviation values are smaller and slope values are closer to zero than the uncorrected test image statistics in Table 1. The slope values for the VIS bands are negative exemplifying that the algorithm over-corrected for sun glint in these bands. The NIR band used in the algorithm was applied to itself setting the spatial profile to the mean deep water ROI radiance value of this band, as depicted by the zero values for standard deviation and slope.

Table 3.   Summary statistics of four VNIR bands from the Lyzenga et al. sun glint corrected image at the deep water ROI pixel locations of (1-320, 3000). The highlighted cell depicts the mean NIR value used in the Lyzenga et al. sun glint correction algorithm.

Band			Lyzenga et al. Sun Glint Corrected Image						
	Wavelength (nm)		Radiance (mW cm^{-2} sr^{-1} μm^{-1}) * 1000						
Color	Peak	Range	Max	Min	Mean	Median	Mode	Standard Deviation	Slope
Blue	460	456-464	2744	1196	1865.340	1849	1832	179.228	-0.253
Green	552	548-555	2407	1022	1544.550	1522	1520	182.831	-0.333
Red	641	637-645	1504	404	938.572	934	939	140.055	-0.324
NIR	860	856-865	494	494	494.000	494	494	0.000	0.000

Figure 21 portrays slope values plotted by wavelength for all bands of the uncorrected test image and the Lyzenga et al. sun glint corrected image. The negative corrected slope values show that the Lyzenga et al. sun glint correction algorithm over-corrected for sun glint in most of the VNIR bands.
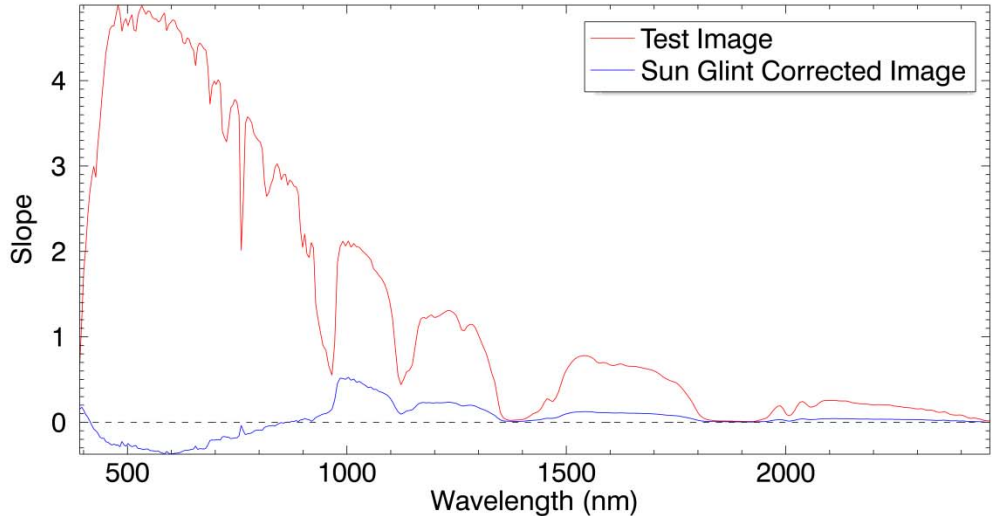
Figure 21.   Plot of slope by wavelength for the test image (red) and the Lyzenga et al. sun glint corrected image (blue).

Figure 22 depicts spectra from a deep water ROI pixel at (1, 3000) with a low amount of sun glint and a deep water ROI pixel at (320, 3000) with a high amount of

sun glint from the Lyzenga et al. sun glint corrected image. The algorithm provided a more correlated match between spectra compared to all other algorithms tested.
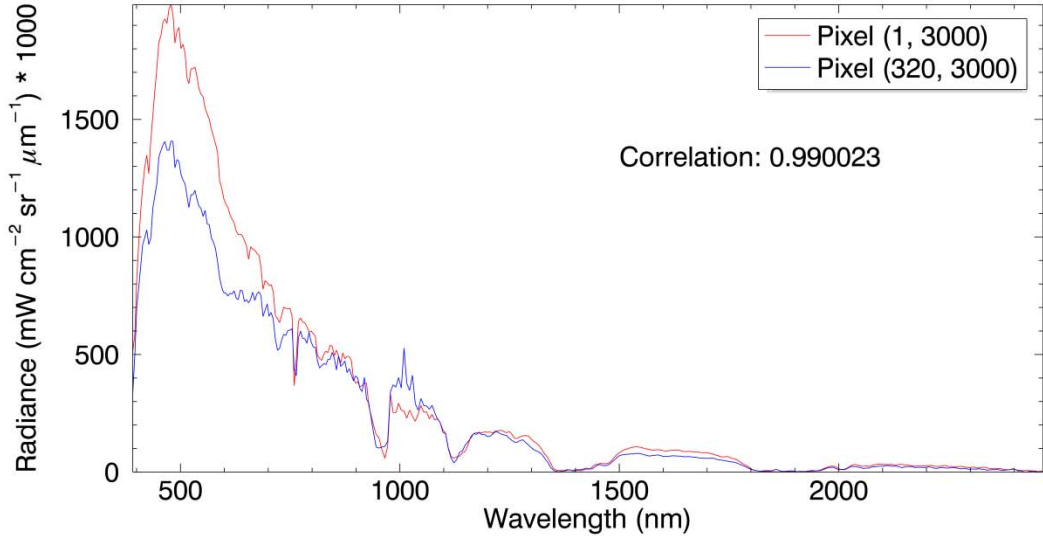
Figure 22.   Spectral plot of radiance by wavelength for a deep water ROI pixel at (1, 3000) with a low amount of glint and a deep water ROI pixel at (320, 3000) with a high amount of glint from the Lyzenga et al. sun glint corrected image.

Figure 23 displays spectra from a deep water ROI pixel at (1, 3000) with a low amount of sun glint from the uncorrected test image and the same pixel in the Lyzenga et al. sun glint corrected image.   The Lyzenga et al. sun glint correction algorithm altered the spectrum of the pixel by increasing the overall radiance of the spectrum from that of the test image spectrum. However, the shape of the spectrum and its spectral features were maintained from the uncorrected test image spectrum.
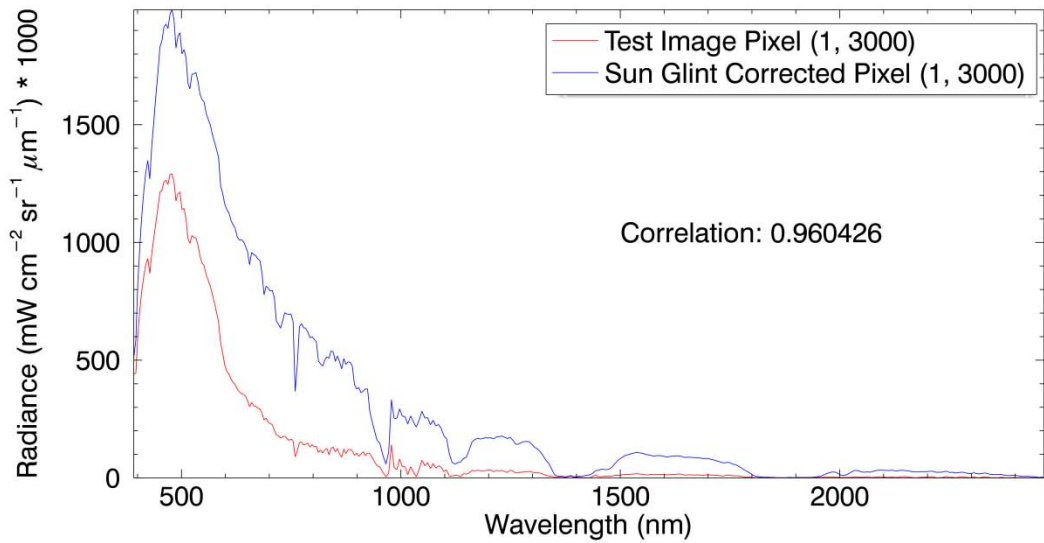
Figure 23.   Spectral plot of radiance by wavelength for a pixel with a low amount of sun glint at the deep water ROI location of (1, 3000) (red) of the test image and a pixel with a low amount of sun glint at the deep water ROI location of (1, 3000) (blue) of the Lyzenga et al. sun glint corrected image.

Figure 24 depicts spectra from a deep water ROI pixel at (320, 3000) with a high amount of sun glint from the uncorrected test image and the same pixel in the Lyzenga et al. sun glint corrected image.   The Lyzenga et al. sun glint correction algorithm increased the overall radiance of spectrum compared to the original image spectrum.   However, the shape of the spectrum and its spectral features were maintained from the original image spectrum.

43
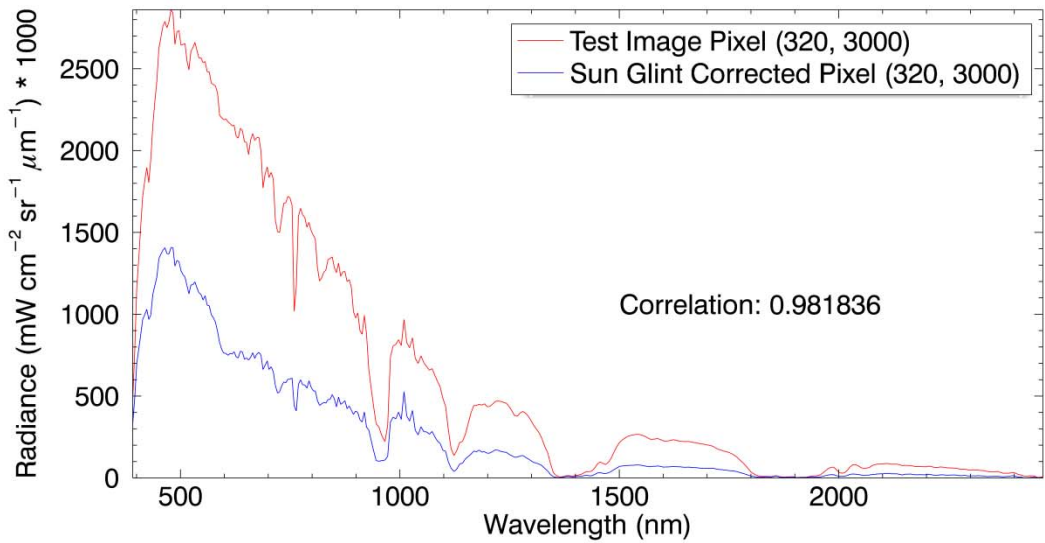
Figure 24.   Spectral plot of radiance by wavelength for a pixel with a high amount of sun glint at the deep water ROI location of (320, 3000) (red) of the test image and a pixel with a high amount of sun glint at the deep water ROI location of (320, 3000) (blue) of the Lyzenga et al. sun glint corrected image.

c.   *Joyce*

Figure 25 provides spatial profiles of four VNIR bands from the Joyce sun glint corrected image for deep water ROI pixel locations of (1-320, 3000).   The radiance variances on the right side of the profiles are smoothed compared to the test image profiles in Figure 12. The dashed lines of the RGB profiles have a weak negative slope while the dashed line of the NIR profile has a flat slope. The NIR profile intersects the y-axis at the modal deep water ROI NIR value used in the algorithm.

44
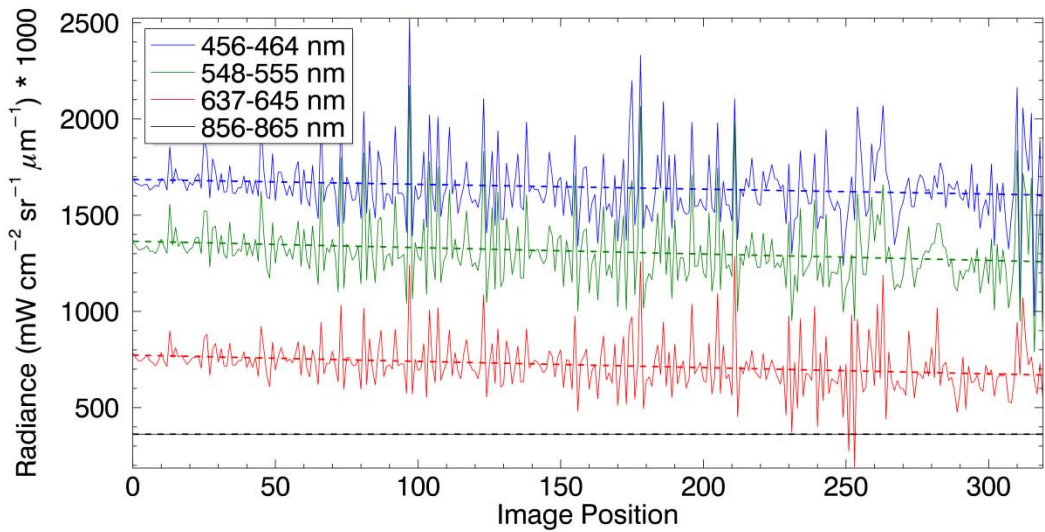
Figure 25.   Spatial profile of four VNIR bands from the Joyce sun glint corrected image at the deep water ROI pixel locations of (1-320, 3000).

Table 4 provides summary statistics of the four VNIR bands in Figure 25. The shaded cell represents the deep water ROI NIR value used in the Joyce sun glint correction algorithm. Standard deviation values are smaller and slope values are closer to zero than the uncorrected test image statistics in Table 1. The slope values for the VIS bands are negative showing that the algorithm over-corrected for sun glint in these bands. The zero values for standard deviation and slope in the NIR band exemplifies that the NIR band used in the algorithm was applied to itself setting the spatial profile to the modal deep water ROI radiance value of this band.

Table 4.   Summary statistics of four VNIR bands from the Joyce sun glint corrected image at the deep water ROI pixel locations of (1-320, 3000). The highlighted cell depicts the modal NIR value used in the Joyce sun glint correction algorithm.

Band			Joyce Sun Glint Corrected Image						
	Wavelength (nm)		Radiance (mW cm^{-2} sr^{-1} μm^{-1}) * 1000						
Color	Peak	Range	Max	Min	Mean	Median	Mode	Standard Deviation	Slope
Blue	460	456-464	2524	976	1645.370	1629	1612	179.223	-0.253
Green	552	548-555	2174	789	1311.700	1289	1287	182.823	-0.333
Red	641	637-645	1504	404	938.572	934	939	140.055	-0.324
NIR	860	856-865	362	362	362.000	362	362	0.000	0.000

Slope values are plotted by wavelength for all bands of the test image and the Joyce sun glint corrected image in Figure 26. The negative corrected slope values explain that the Joyce sun glint correction algorithm over-corrected for sun glint in most of the VNIR bands.
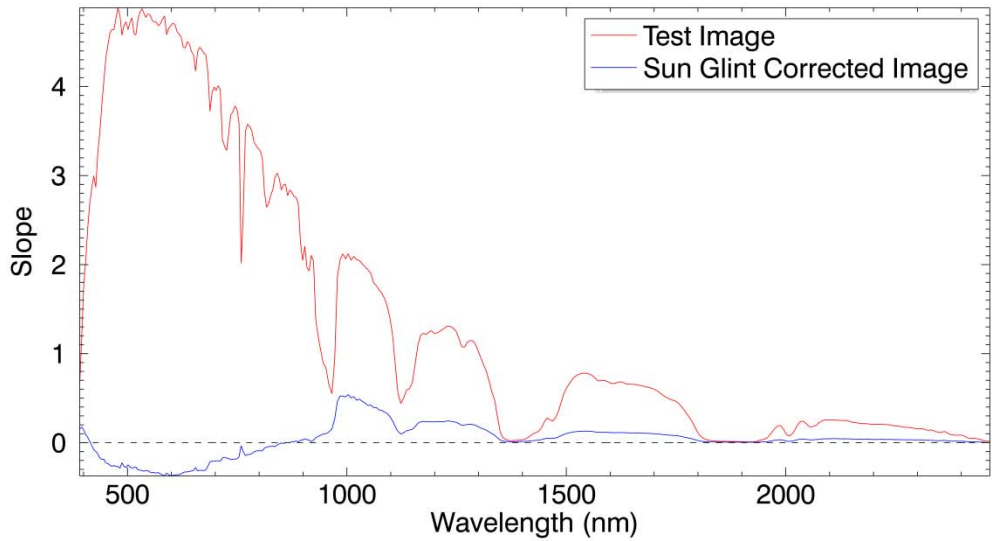
Figure 26.   Plot of slope by wavelength for the uncorrected test image (red) and the Joyce sun glint corrected image (blue).

The spectra from a deep water ROI pixel at (1, 3000) with a low amount of sun glint and a deep water ROI pixel at (320, 3000) with a high amount of sun glint from the Joyce sun glint corrected image are depicted in Figure 27. The algorithm provided a good correlated match between spectra.
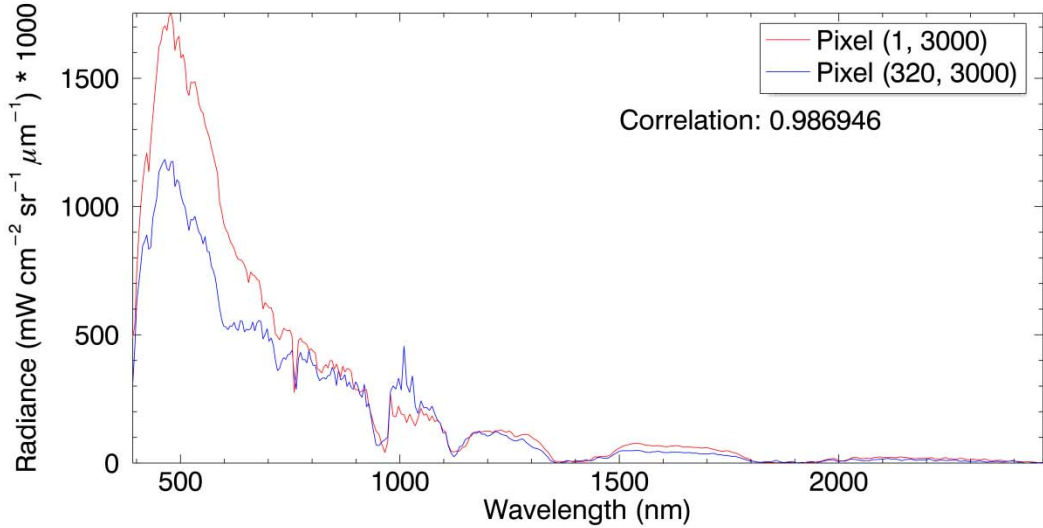

Figure 27.   Spectral plot of radiance by wavelength for a pixel with less sun glint at the deep water ROI location of (1, 3000) (red) and a pixel with more sun glint at the deep water ROI location of (320, 3000) (blue) of the Joyce sun glint corrected image.

Spectra from a deep water ROI pixel at (1, 3000) with a low amount of sun glint from the uncorrected test image and the same pixel in the Joyce sun glint corrected image are provided in Figure 28. The Joyce sun glint correction algorithm altered the spectrum of the pixel by increasing the overall radiance of the spectrum from that of the uncorrected test image spectrum. However, the shape of the spectrum and its spectral features were maintained from the test image spectrum.
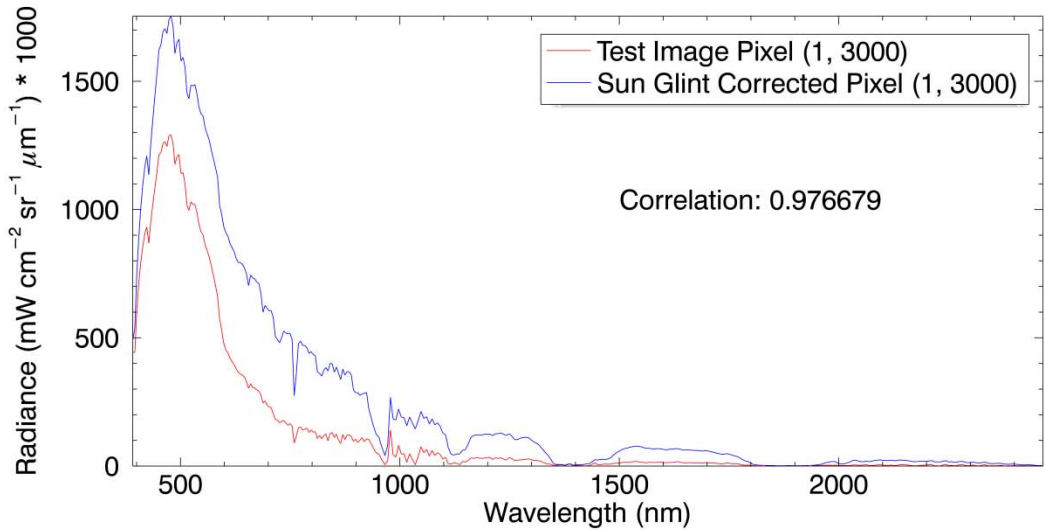
Figure 28.   Spectral plot of radiance by wavelength for a pixel with a low amount of sun
glint at the deep water ROI location of (1, 3000) (red) of the test image and a
pixel with a low amount of sun glint at the deep water ROI location of (1,
3000) (blue) of the Joyce sun glint corrected image.

Spectra from a deep water ROI pixel at (320, 3000) with a high amount of sun glint from the test image is plotted with the same pixel in the Joyce sun glint corrected image in Figure 29.   The Joyce sun glint correction algorithm reduced the overall radiance of spectrum compared to the original image spectrum.   However, the shape of the spectrum and most of its spectral features were maintained from the original image spectrum.
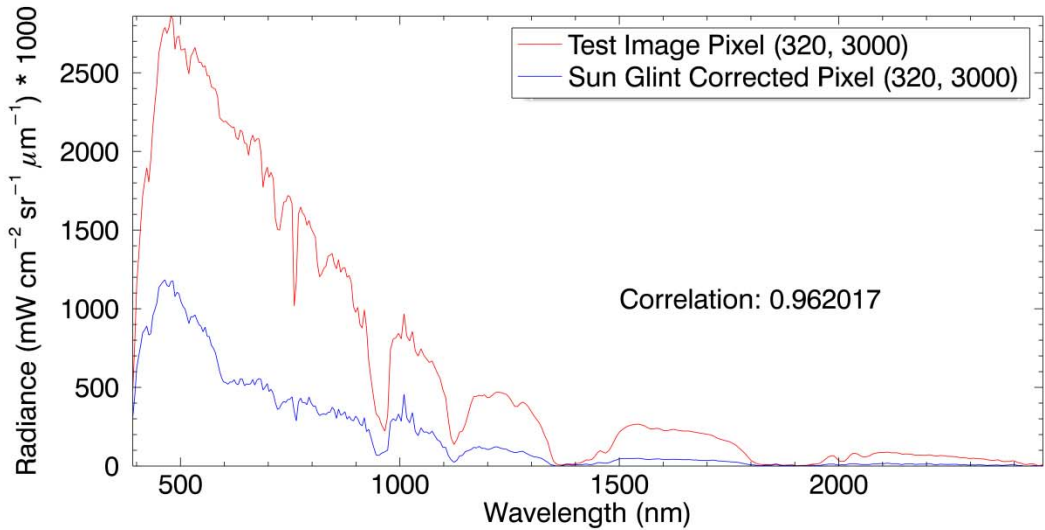
Figure 29.   Spectral plot of radiance by wavelength for a pixel with a high amount of sun glint at the deep water ROI location of (320, 3000) (red) of the test image and a pixel with a high amount of sun glint at the deep water ROI location of (320, 3000) (blue) of the Joyce sun glint corrected image.

d.   *Kuster et al.*

Spatial profiles of four VNIR bands from the Kuster et al. sun glint corrected image for the deep water ROI pixel locations of (1-320, 3000) are provided in Figure 30. The radiance variances on the right side of the spatial profiles are smooth when compared to the test image profiles in Figure 12, but not as smooth as the regression-based spatial profiles. The dashed lines of the VNIR profiles show a weak positive slope.
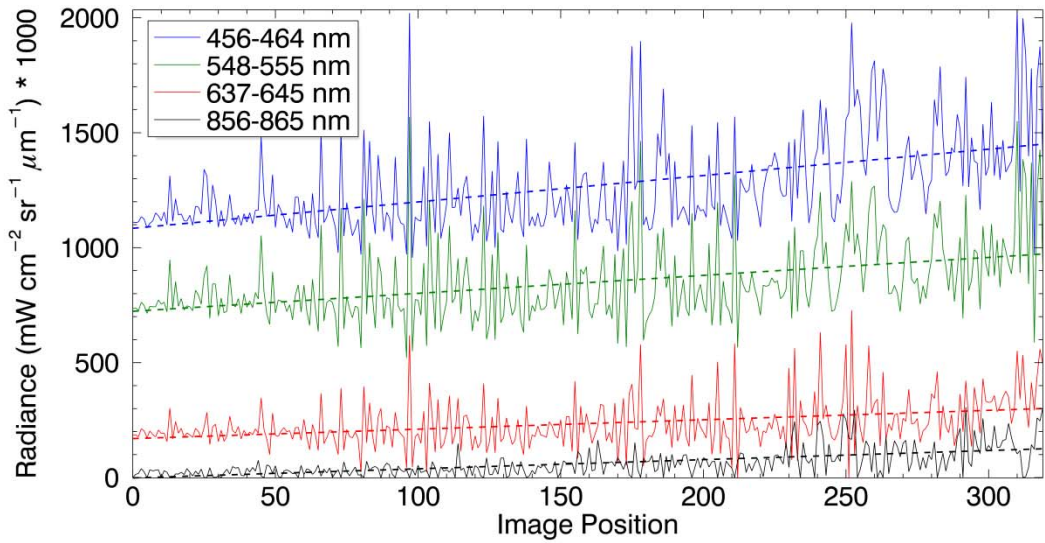
Figure 30.   Spatial profile of four VNIR bands from the Kuster et al. sun glint corrected image at the deep water ROI pixel locations of (1-320, 3000).

Summary statistics of the VNIR bands shown in Figure 30 are provided in Table 5. Standard deviation values are smaller and slope values are closer to zero than the uncorrected test image statistics in Table 1, although they are not as small or as close to zero than the regression-based algorithms. The slope values for the VNIR bands are positive depicting that the algorithm under-corrected for sun glint in these bands.

Table 5.   Summary statistics of four VNIR bands from the Kuster et al. sun glint corrected image at the deep water ROI pixel locations of (1-320, 3000).

Band			Kuster et al. Sun Glint Corrected Image						
	Wavelength (nm)		Radiance (mW cm^{-2} sr^{-1} μm^{-1}) * 1000						
Color	Peak	Range	Max	Min	Mean	Median	Mode	Standard Deviation	Slope
Blue	460	456-464	2035	956	1267.350	1192	1116	208.351	1.147
Green	552	548-555	1569	521	847.903	801	706	177.372	0.781
Red	641	637-645	728	0	234.809	206	203	110.646	0.410
NIR	860	856-865	306	0	61.778	43	0	62.218	0.397

Figure 31 illustrates slope values plotted by wavelength for all bands of the uncorrected test image and the Kuster et al. sun glint corrected image. The slope values for the Kuster et al. sun glint corrected image are positive exemplifying that the algorithm did not over-corrected for sun glint in any of the bands.
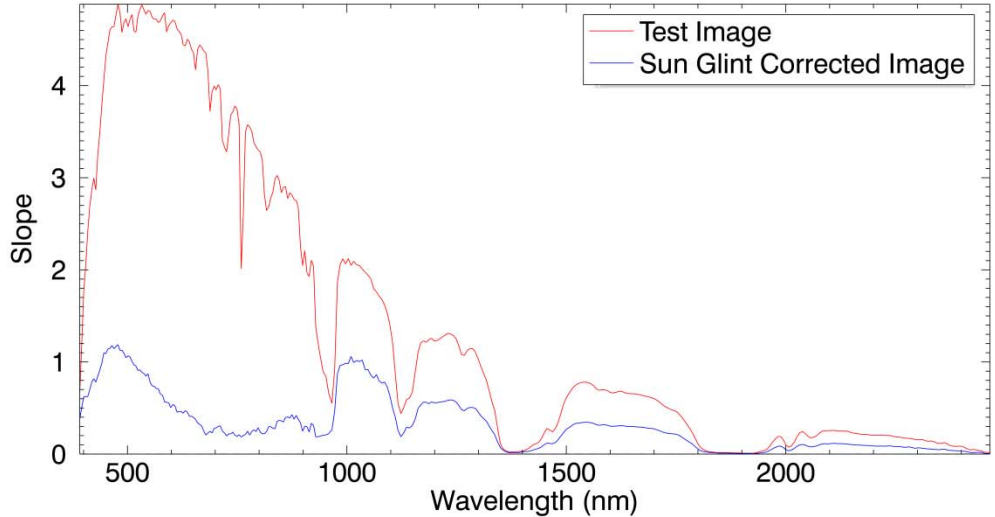

Figure 31.   Plot of slope by wavelength for the test image (red) and the Kuster et al. sun glint corrected image (blue).

Spectra from a deep water ROI pixel at (1, 3000) with a low amount of sun glint and a deep water ROI pixel at (320, 3000) with a high amount of sun glint from the Kuster et al. sun glint corrected image are depicted in Figure 32. This algorithm performed the best at matching the overall radiance between the two spectra in the VIS bands. However, there is a larger difference between radiance levels between the two spectra in the NIR and SWIR regions compared to the regression-based algorithms.
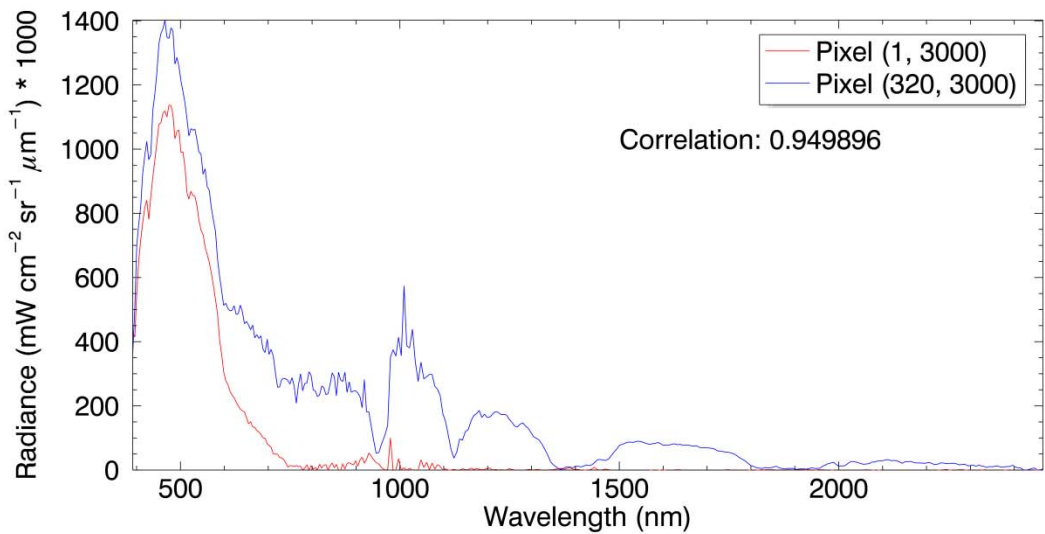
Figure 32.   Spectral plot of radiance by wavelength for a pixel with less sun glint at the deep water ROI location of (1, 3000) (red) and a pixel with more sun glint at the deep water ROI location of (320, 3000) (blue) of the Kuster et al. sun glint corrected image.

Figure 33 provides spectra from a deep water ROI pixel at (1, 3000) with a low amount of sun glint from the test image and the same pixel in the Kuster et al. sun glint corrected image. The Kuster et al. sun glint correction algorithm slightly altered the spectrum of the pixel in the VIS and SWIR bands. However, the shapes of the spectra differ in the NIR region with the corrected spectra losing the 760 nm oxygen absorption feature.
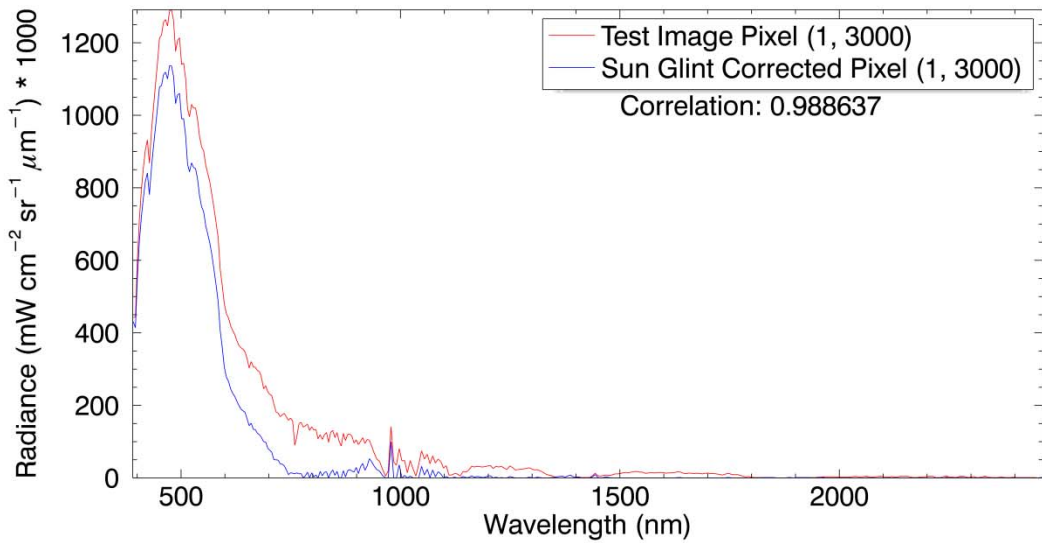
Figure 33.   Spectral plot of radiance by wavelength for a pixel with a low amount of sun glint at the deep water ROI location of (1, 3000) (red) of the test image and a pixel with a low amount of sun glint at the deep water ROI location of (1, 3000) (blue) of the Kuster et al. sun glint corrected image.

Figure 34 shows spectra from a deep water ROI pixel at (320, 3000) with a high amount of sun glint from the test image and the same pixel in the Kuster et al. sun glint corrected image. The Kuster et al. sun glint correction algorithm reduced the overall radiance of the spectrum compared to the original image spectrum. However, some of the spectral features were lost in the corrected spectrum including the 760 nm oxygen absorption feature.
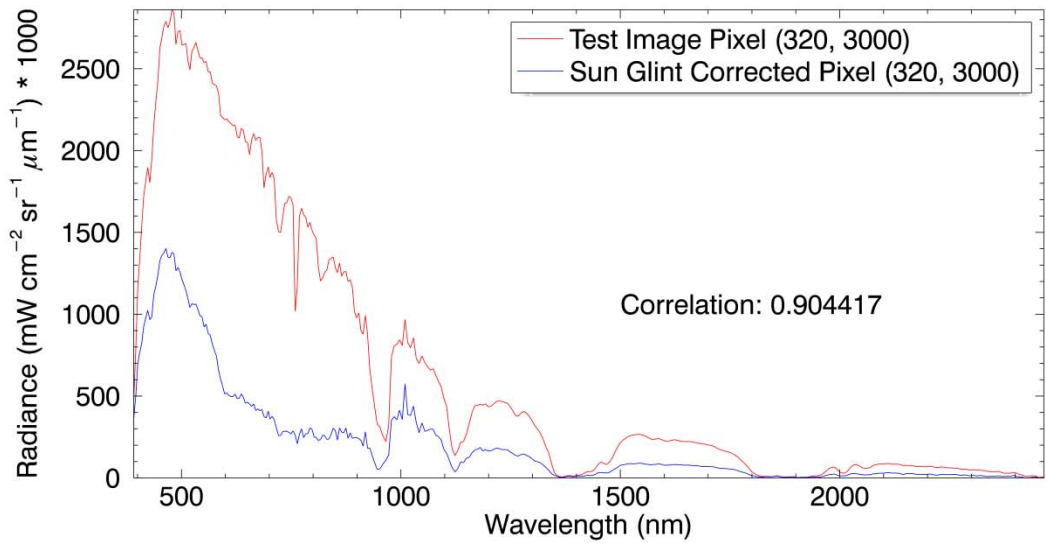
Figure 34.   Spectral plot of radiance by wavelength for a pixel with a high amount of sun glint at the deep water ROI location of (320, 3000) (red) of the test image and a pixel with a high amount of sun glint at the deep water ROI location of (320, 3000) (blue) of the Kuster et al. sun glint corrected image.

The results of the various spectral comparisons of the sun glint correction methods are provided in Table 6. The averaged correlation values for the spectral comparison tests resulted in the Lyzenga et al. sun glint correction algorithm outperforming the rest of the algorithms. The Joyce algorithm is in close second place behind the Lyzenga et al. algorithm. The Kuster et al. and the Hedley et al. algorithms are a distant third and fourth place, respectively.

Table 6.   Spectral comparison results of the tested sun glint correction algorithms. The grey highlighted cells depict the highest correlation values and the yellow highlighted cells depict the lowest correlation values for each comparison.

Correlation	Hedley et al.	Lyzenga et al.	Joyce	Kuster et al.
Sun Glint Corrected Pixel (1, 3000) vs. Sun Glint Corrected Pixel (320, 3000)	0.959854	0.990023	0.986946	0.949896
Uncorrected Test Image Pixel (1, 3000) vs. Sun Glint Corrected Pixel (1, 3000)	0.999997	0.960426	0.976679	0.988637
Uncorrected Test Image Pixel (320, 3000) vs. Sun Glint Corrected Pixel (320, 3000)	0.78858	0.981836	0.962017	0.904417
Average	0.916144	0.977428	0.975214	0.947650
Rank	4th	1st	2nd	3rd

THIS PAGE INTENTIONALLY LEFT BLANK

V. CONCLUSIONS AND FUTURE WORK

A. CONCLUSIONS

The regression-based methods over-corrected for sun glint in the VNIR bands, although they outperformed the Kuster et al. algorithm. Visually, the Kuster et al. algorithm left the highest amount of glint in the image compared to the regression-based methods. If the tests in this thesis were strictly a MSI exercise, any one of the regression-based algorithms would be a good candidate for use due to their similar performance. They differ in their ability to maintain spectral integrity. The Hedley et al. algorithm did not alter the spectrum of the deep water ROI pixel at (1, 3000) with a low amount of glint. However, it drastically altered the pixel with a high amount of glint at the deep water ROI location of (320, 3000). The Lyzenga et al. algorithm changed the spectrum of the deep water ROI pixel at (1, 3000) more so than all other tested algorithms. It performed the best, however, at maintaining the spectral features of the corrected spectrum for the pixel with a high amount of glint. The Joyce algorithm consistently performed well and maintained the spectral integrity of the corrected spectra.

Based on the testing provided in this thesis, the Lyzenga et al. sun glint correction algorithm received the highest average correlation value of 0.977 and is recommended for correction of sun glint in hyperspectral imagery when spectral integrity of the corrected image is required.

B. FUTURE WORK

The sun glint correction algorithms tested in this thesis may not perform similarly for all images and all situations. The tested algorithms may not perform well on wave-induced sun and sky glint. The development of new methods to reduce ocean surface clutter may perform better in these situations. One such development involves using wave gravity energy in the frequency domain to reduce ocean surface clutter (R. Abileah and Z. Bergen, personal communication, April 18, 2012). This new method shows promise, but more research needs to be conducted to determine its utility to HSI applications.

THIS PAGE INTENTIONALLY LEFT BLANK

APPENDIX A.   HEDLEY ET AL. SUN GLINT CORRECTION ALGORITHM

```
; docformat = 'rst'
;+
; NAME:
; hedley.pro
;
; PURPOSE:
; This procedure performs the sun glint correction method
; from Hedley et al. (2005) on a hyperspectral image.
;
; INPUTS:
; Hyperspectral image with the NIR band used in the
; correction in the 100th index.  If the 100th index band
; is not desired, change the NIRIndex variable to the
; desired NIR band index.  ENVI ROI file of deep water
; pixels.
;
; OUTPUTS:
; Hyperspectral image with sun glint corrected.  The
; output will be in BIL format with 16-bit unsigned
; integer pixel values.
;
; SIDE EFFECTS:
; The NIR band used for the sun glint correction will be
; unusable in the output image.
;
; MODIFICATION HISTORY:
;   Written by: Chad Miller, Research Assistant, Remote
;   Sensing Center, Naval Postgraduate School, 8/4/2012.
;   Modified from code written by Zachary Bergen, Goodrich
;   Corporation, 4/1/2012
;-
pro hedley
  compile_opt idl2

  ;Begin ENVI batch mode
  envi, /restore_base_save_files
  envi_batch_init

  ;User defined input image
  filename = $
  dialog_pickfile(/read, title = 'Select an image file for input')

  ;Open image with ENVI library routines
  envi_open_file, filename, r_fid = fid
  ;Read ENVI header and set variables
  envi_file_query, $
    fid, dims = dims, nb = nb, nl = nl, ns = ns
  ;Create index array where size is equal to number of
  ;bands in image
  pos = indgen(nb)
```

```
;Index value of the NIR band used in sun glint correction.
;Change this to desired NIR band index
NIRIndex = 100

;Initialize data input variable
data = uintarr(ns, nb, nl)
;Read input image into variable
for band1 = 0, nb - 1 do begin
  data[*, band1, *] = $
    envi_get_data(fid = fid, pos = band1, dims = dims)
endfor

;User defined ROI file
ROIFile = $
dialog_pickfile(/read, title = 'Select ROI File of Glint Pixels')
;Read ROI file using ENVI library routines
envi_restore_rois, ROIFile
roi_id = $
envi_get_roi_ids(roi_names = roi_names, roi_colors = roi_colors)
;Apply ROI to input image variable and create ROI data variable
dataROI = envi_get_roi_data(roi_id[0], fid = fid, pos = pos)

;Create vector of NIR band ROI pixels
nirLinear = reform(dataROI[NIRIndex, *])
;Find the minimum NIR ROI value and put into variable
minNIR = min(nirLinear)

;Initialize slope vector
slopeVec = fltarr(nb)
;For all bands
for band2 = 0, nb - 1 do begin
  ;Create ROI vector of band
  linear = reform(dataROI[band2, *])
  ;Find slope of regression line using the NIR ROI vector
  ;to ROI vector of band
  res = regress(nirLinear, linear)
  ;Populate slope vector
  slopeVec[band2] = res
endfor

;Initialize sun glint corrected image as 16-bit BIL file
deGlintImage = uintarr(ns, nb, nl)
;For every pixel and for every band perform sun glint correction
;algorithm
for line = 0, nl - 1 do begin
  for samp = 0, ns - 1 do begin
    for band3 = 0, nb - 1 do begin
      ;Subtract the product of the slope vector and  the NIR minus
      ;the minimum NIR value from the input image
      result = data[samp, band3, line] - slopeVec[band3] * $
        (data[samp, NIRIndex, line] - minNIR)
      ;Set negative values to zero
      if (result lt 0) then result = 0
      ;Round floating point values to integers
```

```
        round_result = round(result)
        ;Populate sun glint corrected image
        deGlintImage[samp, band3, line] = round_result
      endfor
    endfor
  endfor

  ;User defined output file
  outfile = $
  dialog_pickfile(/write, title = 'Enter the output filename ')
  ;Write sun glint corrected image to file
  openw, lun, outfile, /get_lun
  writeu, lun, deGlintImage
  free_lun, lun

end
```

THIS PAGE INTENTIONALLY LEFT BLANK

APPENDIX B.   LYZENGA ET AL. SUN GLINT CORRECTION ALGORITHM

```
; docformat = 'rst'
;+
; NAME:
; lyzenga.pro
;
; PURPOSE:
; This procedure performs the sun glint correction method from
; Lyzenga et al. (2006) on a hyperspectral image.
;
; INPUTS:
; Hyperspectral image with the NIR band used in the correction
; in the 100th index.  If the 100th index band is not desired,
; change the NIRIndex variable to the desired NIR band index.
; ENVI ROI file of deep water pixels.
;
; OUTPUTS:
; Hyperspectral image with sun glint corrected.  The output will be
; in BIL format with 16-bit unsigned integer pixel values.
;
; SIDE EFFECTS:
; The NIR band used for the sun glint correction will be unusable
; in the output image.
;
; MODIFICATION HISTORY:
;   Written by: Chad Miller, Research Assistant, Remote Sensing
;   Center, Naval Postgraduate School, 8/4/2012.
;-
pro lyzenga
  compile_opt idl2

  ;Begin ENVI batch mode
  envi, /restore_base_save_files
  envi_batch_init

  ;User defined input image
  filename = $
  dialog_pickfile(/read, title = 'Select an image file for input')

  ;Open image with ENVI library routines
  envi_open_file, filename, r_fid = fid
  ;Read ENVI header and set variables
  envi_file_query, fid, dims = dims, nb = nb, nl = nl, ns = ns
  ;Create index array where size is equal to number of bands
  ;in image
  pos = lindgen(nb)

  ;Index value of the NIR band used in sun glint correction.
  ;Change this to desired NIR band index
  NIRIndex = 100
```

```
;Initialize data input variable
data = uintarr(ns, nb, nl)
;Read input image into variable
for band = 0, nb - 1 do begin
  data[*, band, *] = $
    envi_get_data(fid = fid, pos = band, dims = dims)
endfor

;User defined ROI file
ROIFile = $
dialog_pickfile(/read, title = 'Select ROI File of Glint Pixels')
;Read ROI file using ENVI library routines
envi_restore_rois, ROIFile
roi_id = $
envi_get_roi_ids(roi_names = roi_names, roi_colors = roi_colors)
;Apply ROI to input image variable and create ROI data variable
dataROI = envi_get_roi_data(roi_id[0], fid = fid, pos = pos)

;Create vector of NIR band ROI pixels
nirLinear = reform(dataROI[NIRIndex,*])
;Find the mean NIR ROI value and put into variable
meanNIR = mean(nirLinear)
;Find variance of NIR ROI pixels and put into variable
varNir = variance(nirLinear)

;Initialize the coefficient vector
coeffVec = fltarr(nb)
;For every band
for index2 = 0, nb - 1 do begin
  ;Create ROI vector of band
  linear = reform(dataROI[index2,*])
  ;Find the covariance of the band's ROI vector to the
  ;NIR ROI vector
  cov = correlate(linear, nirLinear, /covariance)
  ;Divide the covariance by the NIR ROI variance
  coeff = cov / varNIR
  ;Populate the coefficient vector
  coeffVec[index2] = coeff
endfor

;Initialize sun glint corrected image as 16-bit BIL file
deGlintImage = uintarr(ns, nb, nl)
;For every pixel and for every band perform sun glint
;correction algorithm
for line = 0, nl - 1 do begin
  for samp = 0, ns - 1 do begin
    for band2 = 0, nb - 1 do begin
      ;Subtract the product of the slope vector and  the NIR minus
      ;the mean NIR value from the input image
      result = data[samp, band2, line] - coeffVec[band2] * $
        (data[samp, NIRIndex, line] - meanNIR)
      ;Set negative values to zero
      if (result lt 0) then result = 0
      ;Round floating point values to integers
      round_result = round(result)
```

64

```
            ;Populate sun glint corrected image
            deGlintImage[samp, band2, line] = round_result
        endfor
    endfor
  endfor

  ;User defined output file
  outfile = $
  dialog_pickfile(/write, title = 'Enter the output filename ')
  ;Write sun glint corrected image to file
  openw, lun, outfile, /get_lun
  writeu, lun, deGlintImage
  free_lun, lun

end
```

THIS PAGE INTENTIONALLY LEFT BLANK

APPENDIX C.   JOYCE SUN GLINT CORRECTION ALGORITHM

```
; docformat = 'rst'
;+
; NAME:
; joyce.pro
;
; PURPOSE:
; This procedure performs the sun glint correction method from
; Joyce (2004) on a hyperspectral image.  Same algorithm as
; Hedley et al. (2005) except uses mode NIR value
; instead of minimum
;
; INPUTS:
; Hyperspectral image with the NIR band used in the correction
; in the 100th index.  If the 100th index band is not desired,
; change the NIRIndex variable to the desired NIR band index.
; ENVI ROI file of deep water pixels.
;
; OUTPUTS:
; Hyperspectral image with sun glint corrected.  The output will be
; in BIL format with 16-bit unsigned integer pixel values.
;
; SIDE EFFECTS:
; The NIR band used for the sun glint correction will be unusable
; in the output image.
;
; MODIFICATION HISTORY:
;   Written by: Chad Miller, Research Assistant, Remote Sensing
;   Center, Naval Postgraduate School, 8/4/2012.
;-
pro joyce
  compile_opt idl2

  ;Begin ENVI batch mode
  envi, /restore_base_save_files
  envi_batch_init

  ;User defined input image
  filename = $
  dialog_pickfile(/read, title = 'Select an image file for input')

  ;Open image with ENVI library routines
  envi_open_file, filename, r_fid = fid
  ;Read ENVI header and set variables
  envi_file_query, fid, dims = dims, nb = nb, nl = nl, ns = ns
  ;Create index array where size is equal to number of bands
  ;in image
  pos = indgen(nb)

  ;Index value of the NIR band used in sun glint correction.
  ;Change this to desired NIR band index
  NIRIndex = 100
```

```
;Initialize data input variable
data = uintarr(ns, nb, nl)
;Read input image into variable
for band1 = 0, nb - 1 do begin
  data[*, band1, *] = $
    envi_get_data(fid = fid, pos = band1, dims = dims)
endfor

;User defined ROI file
ROIFile = $
dialog_pickfile(/read, title = 'Select ROI File of Glint Pixels')
;Read ROI file using ENVI library routines
envi_restore_rois, ROIFile
roi_id = $
envi_get_roi_ids(roi_names = roi_names, roi_colors = roi_colors)
;Apply ROI to input image variable and create ROI data variable
dataROI = envi_get_roi_data(roi_id[0], fid = fid, pos = pos)

;Create vector of NIR band ROI pixels
nirLinear = reform(dataROI[NIRIndex, *])
;Copy vector into sort vector
nirLinear_sort = nirLinear

;Find the mode NIR ROI value and put into variable
nirLinear_sort = nirLinear_sort[bsort(nirLinear_sort)]
wh = where(nirLinear_sort ne shift(nirLinear_sort, -1), cnt)
if cnt eq 0 then modeNIR = nirLinear_sort[0] else begin
  void = max(wh - [-1, wh], mxpos)
  modeNIR = long(nirLinear_sort[wh[mxpos]])
endelse

;Initialize slope vector
slopeVec = fltarr(nb)
;For all bands
for band2 = 0, nb - 1 do begin
  ;Create ROI vector of band
  linear = reform(dataROI[band2, *])
  ;Find slope of regression line using the NIR ROI vector
  ;to ROI vector of band
  res = regress(nirLinear, linear)
  ;Populate slope vector
  slopeVec[band2] = res
endfor

;Initialize sun glint corrected image as 16-bit BIL file
deGlintImage = uintarr(ns, nb, nl)
;For every pixel and for every band perform sun glint correction
;algorithm
for line = 0, nl - 1 do begin
  for samp = 0, ns - 1 do begin
    for band3 = 0, nb - 1 do begin
      ;Subtract the product of the slope vector and  the NIR minus
      ;the modal NIR value from the input image
      result = data[samp, band3, line] - slopeVec[band3] * $
```

68

```
          (data[samp, NIRIndex, line] - modeNIR)
        ;Set negative values to zero
        if (result lt 0) then result = 0
        ;Round floating point values to integers
        round_result = round(result)
        ;Populate sun glint corrected image
        deGlintImage[samp, band3, line] = round_result
      endfor
    endfor
  endfor

  ;User defined output file
  outfile = $
  dialog_pickfile(/write, title = 'Enter the output filename ')
  ;Write sun glint corrected image to file
  openw, lun, outfile, /get_lun
  writeu, lun, deGlintImage
  free_lun, lun

end
```

THIS PAGE INTENTIONALLY LEFT BLANK

APPENDIX D.   KUSTER ET AL. SUN GLINT CORRECTION ALGORITHM

```
; docformat = 'rst'
;+
; NAME:
; kuster.pro
;
; PURPOSE:
; This procedure performs the sun glint correction method from
; Kuster et al. (2009) on a hyperspectral image.
;
; INPUTS:
; Hyperspectral image and index values for the 750, 760,
; and 775 nm bands.  Change the index values to those specified
; for the desired input image.  ENVI ROI file of deep water pixels.
;
; OUTPUTS:
; Hyperspectral image with sun glint corrected.  The output will be
; in BIL format with 16-bit unsigned integer pixel values.
;
; MODIFICATION HISTORY:
;    Written by: Chad Miller, Research Assistant, Remote Sensing
;    Center, Naval Postgraduate School, 8/4/2012.
;-
pro kuster
  compile_opt idl2

  ;Begin ENVI batch mode
  envi, /restore_base_save_files
  envi_batch_init

  ;User defined input image
  filename = $
  dialog_pickfile(/read, title = 'Select an image file for input')

  ;Open image with ENVI library routines
  envi_open_file, filename, r_fid = fid
  ;Read ENVI header and set variables
  envi_file_query, fid, dims = dims, nb = nb, nl = nl, ns = ns
  ;Create index array where size is equal to number of bands in
  ;image
  pos = lindgen(nb)

  ;Change these values for other data sets
  ;Set the index value of the 750 nm band
  Index750 = 77
  ;Set the index value of the 760 nm band
  Index760 = 79
  ;Set the index value of the 775 nm band
  Index775 = 82

  ;Initialize data input variable
```

```
data = uintarr(ns, nb, nl)
;Read input image into variable
for band = 0, nb - 1 do begin
  data[*, band, *] = $
    envi_get_data(fid = fid, pos = band, dims = dims)
endfor

;User defined ROI file
ROIFile = $
dialog_pickfile(/read,title = 'Select ROI File of Glint Pixels')
;Read ROI file using ENVI library routines
envi_restore_rois, ROIFile
roi_id = $
envi_get_roi_ids(roi_names = roi_names, roi_colors = roi_colors)
;Apply ROI to input image variable and create ROI data variable
dataROI = $
envi_get_roi_data(roi_id[0], fid = fid, pos = pos, addr = addr)

;Find the size of the input image ROI
ROI_pts = size(dataROI)
;Find the total number of pixels in on band of input image ROI
ROI_vec = ROI_pts[2]
;Calculate the x coordinates of input image ROI
dataROI_samp = (addr mod ns)
;Calculate the y coordinates of input image ROI
dataROI_line = (addr / ns)

;Initialize depth image
d_image = fltarr(ns, 1, nl)
;For every spectrum of input image
for samp = 0, ns - 1 do begin
  for line = 0, nl - 1 do begin
    ;Calculate 760 nm oxygen absorption depth
    d_image[samp, 0, line] = ((data[samp, Index750, line] + $
    data[samp, Index775, line]) / 2) - data[samp, Index760, line]
    ;Set negative values to zero
    if (d_image[samp, 0, line] < 0.0) then $
      d_image[samp, 0, line] = 0.0
  endfor
endfor

;Initialize ROI vector of depth image
d_imageROI = uintarr(ROI_vec)
;Apply ROI to depth image
for i = 0, ROI_vec - 1 do begin
  a = d_image[dataROI_samp[i], *, dataROI_line[i]]
  d_imageROI[i] = a
endfor

;Find min/max of depth image ROI including indices
d_max = $
max(d_imageROI, d_max_i, min = d_min, subscript_min = d_min_i)

;Initialize the glint spectral variation spectrum
g = fltarr(1, nb, 1)
```

```
;Create the glint spectral variation spectrum by subtracting the
;minimum ROI depth from the maximum ROI depth for every band of
;the input image
g[*, *, *] = $
data[dataROI_samp[d_max_i], *, dataROI_line[d_max_i]] - $
data[dataROI_samp[d_min_i], *, dataROI_line[d_min_i]]

;Initialize the normalized depth image
d_norm = fltarr(ns, 1, nl)
;For every pixel normalize the depth image
for samp = 0, ns - 1 do begin
  for line = 0, nl - 1 do begin
    ;Normalize every pixel by dividing by the maximum ROI depth
    d_norm[samp, 0, line] = d_image[samp, 0, line] / d_max
  endfor
endfor

;Initialize sun glint corrected image as 16-bit BIL file
deGlintImage = uintarr(ns, nb, nl)
;For every pixel and for every band perform sun glint correction
;algorithm
for samp2 = 0, ns - 1 do begin
  for line2 = 0, nl - 1 do begin
    for band3 = 0, nb - 1 do begin
      ;Subtract the product of the depth normalized image and
      ;glint spectral variation spectrum from the input image
      result = data[samp2, band3, line2] - $
        (g[*, band3, *] * d_norm[samp2, *, line2])
      ;Set negative values to zero
      if (result lt 0) then result = 0
      ;Round floating point values to integers
      round_result = round(result)
      ;Populate sun glint corrected image
      deGlintImage[samp2, band3, line2] = round_result
    endfor
  endfor
endfor

;User defined output file
outfile = $
dialog_pickfile(/write, title='Enter the output filename ')
;Write sun glint corrected image to file
openw, lun, outfile, /get_lun
writeu, lun, deGlintImage
free_lun, lun

end
```

THIS PAGE INTENTIONALLY LEFT BLANK

LIST OF REFERENCES

Berk, Alexander, Lawrence S. Bernstein, and David C. Robertson. *MODTRAN: A moderate resolution model for LOWTRAN 7.* Final Report, Hanscomb AFB, MA: United States Air Force Geophysical Laboratory, 1989.

Bukata, Robert P., John H. Jerome, Kirill Ya. Kondratyev, and Dimitry V. Posdnyakov. *Optical Properties and Remote Sensing of Inland and Coastal Waters.* Boca Raton, FL: CRC Press, 1995.

Burns, Roger G. *Mineralogical Applications of Crystal Field Theory, Second Edition.* Cambridge, MA: Cambridge University Press, 1993.

Campbell, James B. *Introduction to Remote Sensing.* New York, NY: The Guilford Press, 1996.

Chandrasekhar, S. *Radiative Transfer.* New York, NY: Dover Publications, 1960.

Clark, Roger N. "Chapter 1: Spectroscopy of Rocks and Minerals, and Principles of Spectroscopy." In *Manual of Remote Sensing, Volume 3, Remote Sensing for the Earth Sciences*, by Andrew N. Rencz, 3-58. New York, NY: John Wiley & Sons, 1999.

Cox, C., and W. Munk. "Statistics of the Sea Surface Derived from Sun Glitter." *Journal of Marine Research*, 1954, 13: 198–227.

Feynman, Richard P. *QED: The Strange Theory of Light and Matter.* Princeton, NJ: Princeton University Press, 1985.

Frohlich, C. "Data on total and spectral solar irradiance: comments." *Applied Optics*, 1983, 22: 3928.

Fukushima, Hajime, Toratani Mitsuhiro, Hiroshi Murakami, Pierre-Yves Deschamps, Robert Frouin, and Akihiko Tanaka. "Evaluation of ADEOS-II GLI Ocean Color Atmospheric Correction Using SIMBADA Handheld Radiometer Data." *Journal of Oceanography*, 2007, 63: 533–543.

Gibson, Paul J. *Introductory Remote Sensing - Principles and Concepts.* London, U.K.: Routledge, 2000.

Goetz, Alexander F. H., Gregg Vane, Jerry E. Solomon, and Barrett N. Rock. "Imaging Spectrometry for Earth Remote Sensing." *Science*, 1985, 228: 1147–1153.

Goodman, James A., ZhongPing Lee, and Susan L. Ustin. "Influence of atmospheric and sea-surface corrections on retrieval of bottom depth and reflectance using a semi-analytical model: a case study in Kaneohe Bay, Hawaii." *Applied Optics*, 2008, 47: F1–F11.

Hecht, Eugene. *Optics: Fourth Edition.* Boston, MA: Addison-Wesley, 2001.

Hedley, J. D., A. R. Harbone, and P. J. Mumby. "Simple and robust removal of sun glint for mapping shallow-water benthos." *International Journal of Remote Sensing*, 2005, 44: 2107–2112.

Hochberg, Eric J., Serge Andrefouet, and Misty R. Tyler. "Sea Surface Correction of High Spatial Resolution Ikonos Images to Improve Bottom Mapping in Near-Shore Environments." *IEEE Transactions on Geoscience and Remote Sensing*, 2003, 41: 1724–1729.

Joyce, K. E. "A Method for Mapping Live Coral Cover Using Remote Sensing." *Ph.D. thesis - University of Queensland, Brisbane, Australia*, 2004.

Kay, Susan, John D. Hedley, and Samantha Lavender. "Sun Glint Correction of High and Low Spatial Resolution Images of Aquatic Scenes: a Review of Methods for Visible and Near-Infrared Wavelengths." *Remote Sensing*, 2009, 1: 697–730.

Kuster, Tiit, Ele Vahtmae, and Jaan Praks. "A sun glint correction method for hyperspectral imagery containing areas with non-neglible water leaving NIR signal." *Remote Sensing of the Environment*, 2009, 113: 2267–2274.

Lee, Zhongping, Kendall L. Carder, Curtis D. Mobley, Robert G. Steward, and Jennifer S. Patch. "Hyperspectral remote sensing for shallow waters: 2. Deriving bottom depths and water properties by optimization." *Applied Optics*, 1999, 38: 3831–3843.

Lyzenga, David R., Norman P. Malinas, and Fred J. Tanis. "Multispectral Bathymetry Using a Simple Physically Based Algorithm." *IEEE Transactions on Geoscience and Remote Sensing*, 2006, 44: 2251–2259.

Mather, Paul M. *Computer processing of remotely-sensed images: an introduction.* West Sussex, England: John Wiley & Sons, Ltd, 2004.

Mobley, Curtis D. *Light and Water, Radiative Transfer in Natural Waters.* San Diego, CA: Academic Press, Inc., 1994.

Montagner, F., V. Billat, and S. Belanger. "MERIS Sun Glint Flag Algorithm." *European Space Agency.* June 10, 2003. http://envisat.esa.int/instruments/meris/atbd/atbd_2_13.pdf (accessed August 29, 2012).

Montes, Marcos J., Bo-Cai Gao, and Curtiss O. Davis. *NRL Atmospheric Correction Algorithms for Oceans: Tafkaa User's Guide.* User's Guide, Washington, DC: United States Navy Naval Research Laboratory, 2004.

Moore, David S., George P. McCabe, Layth C. Alwan, Bruce A. Craig, and William M. Duckworth. *The Practice of Statistics for Business and Economics.* New York, NY: W.H. Freeman and Company, 2011.

Mustard, John F., Matthew I. Staid, and William J. Fripp. "A semianalytical approach to the calibration of AVIRIS data to reflectance over water application in a temperate estuary." *Remote Sensing of the Environment*, 2001, 75: 335–349.

Olsen, Richard C. *Remote Sensing from Air and Space.* Bellingham, Washington: SPIE Press, 2007.

Ottaviani, Matteo, Robert Spurr, Knut Stamnes, Wei Li, Wenying Su, and Warran Wiscombe. "Improving the Description of Sunglint for Accurate Prediction of Remotely Sensed Radiances." *Journal of Quantitative Spectroscopy & Radiative Transfer*, 2008, 109: 2364–2375.

Phillips, Kenneth J.H. *Guide to the Sun.* Cambridge, MA: Cambridge University Press, 1995.

Richards, John A., and Xiuping Jia. *Remote Sensing Digital Image Analysis - An Introduction.* Berlin, Germany: Springer-Verlag Berlin Heidelberg, 2006.

Silva, Dennis, and Ron Abileah. "Two Algorithms for Removing Ocean Surface Clutter in Multispectral and Hyperspectral Images." *Ocean Optics XIV.* Kailua-Kona, Hawaii, 1999.

SpecTIR. "ProSpecTIR VS Specifications." *SpecTIR.* 2011. http://www.spectir.com/wp-content/uploads/2012/02/ProSpecTIR_VS_specs_2011.pdf (accessed August 29, 2012).

Swayze, Gregg A., Roger N. Clark, Alexander F. H. Goetz, Thomas G. Chrien, and Noel S. Gorelick. "Effects of spectrometer band pass, sampling, and signal-to-noise ratio on spectral identification using the tetracorder algorithm." *Journal of Geophysical Research*, 2003, 108: 1–30.

Van Der Meer, Freek D., and Steven M. De Jong. *Imaging Spectrometry: Basic Principles and Prospective Applications.* Dordrecht, Netherlands: Springer, 2006.

Van Mol, Barbara, and Kevin Ruddick. "The Compact High Resolution Imaging Spectrometer (CHRIS): the future of hyperspectral satellite sensors. Imagery of Oostende coastal and inland waters." *Airborne Imaging Spectroscopy Workshop.* Bruges, 2004. 123–125.

Wang, Menghua, and Sean W. Bailey. "Correction of Sun Glint Contamination on the SeaWiFS Ocean and Atmosphere Products." *Applied Optics*, 2001, 40: 4790–4798.

INITIAL DISTRIBUTION LIST

1.   Defense Technical Information Center
        Ft. Belvoir, Virginia

2.   Dudley Knox Library
        Naval Postgraduate School
        Monterey, California

3.   Dr. Richard C. Olsen
        Naval Postgraduate School
        Monterey, California

4.   Dr. Fred A. Kruse
        Naval Postgraduate School
        Monterey, California

5.   Major Neal Hinson
        United States Air Force
        Washington, DC

6.   Mr. Kevin Whitcomb
        UTC Aerospace Systems
        Westford, Massachusetts

7.   Mr. Zachary Bergen
        UTC Aerospace Systems
        Westford, Massachusetts

8.   Mr. Ron Abileah
        jOmegak
        San Carlos, California

9.   Major Joshua Smith
        United States Air Force
        Beale Air Force Base, California

10.   Dr. Dan C. Boger
        Naval Postgraduate School
        Monterey, California